

# A Survey on 3D-aware Image Synthesis

Weihao Xia and Jing-Hao Xue, *Senior Member, IEEE*

**Abstract**—Recent years have seen remarkable progress in deep learning powered visual content creation. This includes 3D-aware generative image synthesis, which produces high-fidelity images in a 3D-consistent manner while simultaneously capturing compact surfaces of objects from pure image collections without the need for any 3D supervision, thus bridging the gap between 2D imagery and 3D reality. The 3D-aware generative models have shown that the introduction of 3D information can lead to more controllable image generation. The task of 3D-aware image synthesis has taken the field of computer vision by storm, with hundreds of papers accepted to top-tier journals and conferences in recent year (mainly the past two years), but there lacks a comprehensive survey of this remarkable and swift progress. Our survey aims to introduce new researchers to this topic, provide a useful reference for related works, and stimulate future research directions through our discussion section. Apart from the presented papers, we aim to constantly update the latest relevant papers along with corresponding implementations at <https://weihaox.github.io/projects/awesome-3d-aware>.

**Index Terms**—Deep Learning, Implicit Neural Representation, Generative models, Computer Vision Survey, Novel View Synthesis



## 1 INTRODUCTION

A tremendous amount of progress has been made in deep generative models that lead to photorealistic image synthesis. Despite achieving compelling results, most approaches focus on two-dimensional (2D) images, overlooking the three-dimensional (3D) nature of the physical world. The lack of 3D structure, therefore, inevitably limits some of their practical applications. Several recent works therefore propose generative models that are 3D-aware, *i.e.*, scenes are modeled in 3D and then rendered differentially to the image plane. In contrast to the 2D generative models, the recently developed 3D-aware generative models [1], [2] bridge the gap between 2D images and 3D physical world. The physical world surrounding us is intrinsically three-dimensional and images depict reality under certain conditions of geometry, material, and illumination, making it natural to model the image generation process in 3D spaces. As shown in Fig. 1, classical rendering (a) renders images at certain camera positions given human-designed or scanned 3D shape models; inverse rendering (b) recovers the underlying intrinsic properties of the 3D physical world from 2D images; 2D image generation (c) is mostly driven by generative models, which have achieved impressive results in photo-realistic image synthesis; 3D-aware image synthesis (d) offers the possibility of replacing the classical rendering pipeline with effective and efficient models that are learned directly from images.

Despite striking progress has been made recently in research of 3D-aware image synthesis, it lacks a timely and systematic review of this progress. In this work, we fill the gap by presenting a comprehensive survey of the latest research in 3D-aware image synthesis methods. We envision that our work will elucidate design considerations and advanced methods for 3D-aware image synthesis, present its advantages and disadvantages of different kinds, and suggest future research directions. We provide an outline and taxonomy of this survey in Fig. 2. We propose to

categorize the 3D-aware image synthesis methods into three categories: 3D control of 2D generative models (Sec. 3), 3D novel view synthesis from multiple views (Sec. 4), and 3D generative models from single views (Sec. 5). Then, every category is further divided into some subcategories depending on the experimental setting or the specific utilization of 3D information. In particular, 3D control of 2D generative models are further divided into 1) 3D control latent directions (Sec. 3.1), 2) 3D parameters as controls (Sec. 3.2), and 3) 3D prior knowledge as constraints (Sec. 3.3). Both Sec. 4 and Sec. 5 summarize the methods that target generating photorealistic and multi-view-consistent images by learning 3D representations. Broadly speaking, both categories leverage neural 3D representations to represent scenes, use differentiable neural renderers to render them into the image plane, and optimize the network parameters by minimizing the difference between rendered images and observed images. However, they are significantly different in training on a multiple-view or single-view image collections, due to their hugely different application scenarios. Moreover, in order to present these representative generative 3D-aware image synthesis methods intuitively, we show a chronological overview in Fig. 3 by organizing them into the three aforementioned paradigms.

Here, we present a timely up-to-date overview of the growing field of 3D-aware image synthesis. Considering the lack of a comprehensive survey and an increasing interest and popularity, we believe it necessary to organize one to help computer vision practitioners with this emerging topic. The purpose of this survey is to provide researchers new to the field with a comprehensive understanding of 3D-aware image synthesis methods and show the superior performance over the status quo approaches. To conclude, we highlight several open research directions and problems that need further investigation. The scope of this fast-expanding field is rather extensive and a panoramic review would be challenging. We shall present only representative methods of 3D-aware image synthesis rather than listing exhaustively all literature. This review can therefore serve as a pedagogical tool, providing researchers with the key

- W. Xia and J.-H. Xue are with the Department of Statistical Science, University College London, London, UK.  
E-mail: [xiawh3@outlook.com](mailto:xiawh3@outlook.com), [jinghao.xue@ucl.ac.uk](mailto:jinghao.xue@ucl.ac.uk)

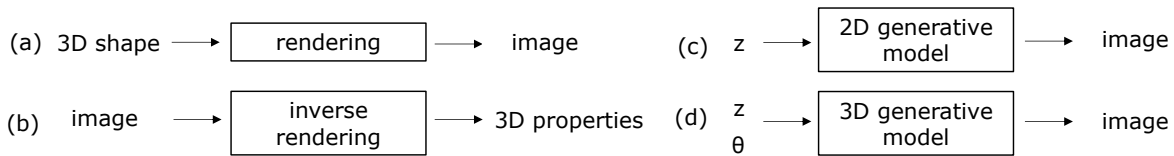


Fig. 1. Comparison of (a) rendering and (b) inverse rendering, (c) 2D generative models and (d) 3D generative models. 3D generative models first learn 3D representations and then render a 2D image at certain viewpoints. Both 2D and 3D generative models have unconditional and conditional settings. An unconditional generative model maps a noise input  $z$  (and a camera pose in 3D models) to a fake image where  $z$  is usually a realization of a Gaussian random variable; a conditional model takes an additional input as the control signal, which could be another image, text, or a categorical label.

information about typical methods of 3D-aware image synthesis. Researchers can use these general guidelines to develop the most appropriate technique for their own particular study. The main technical contributions of this work are as follows:

- **Hierarchical taxonomy.** We propose a systematic taxonomy for 3D-aware image synthesis research. We categorize existing models into three categories: 3D control of 2D generative models, 3D generative models from single views, and novel view synthesis from multiple views.
- **Comprehensive review.** We provide a comprehensive overview of the existing state-of-the-art 3D-aware image synthesis methods. We compare and analyze the main characteristics and improvements for each type, assessing their strengths and weaknesses.
- **Outstanding challenges.** We present open research problems and provide some suggestions for the future development of 3D-aware image synthesis.
- **In an attempt to continuously track recent developments** in this fast advancing field, we provide an accompanying webpage which catalogs papers addressing 3D-aware image synthesis, according to our problem-based taxonomy: <https://weihaox.github.io/projects/awesome-3d-aware>.

## 2 BACKGROUND

This section introduces a few important concepts as the background. In order to formulate 3D-aware image synthesis, we first clarify how 2D and 3D data are expressed, and how they are converted between each other. Moreover, we introduce two key elements involved in most 3D-aware image synthesis methods: implicit neural representations and differentiable neural rendering.

### 2.1 2D and 3D Data, Rendering and Inverse Rendering

The 2D images depict a glimpse into the surrounding 3D physical world with its geometry, materials, and illumination conditions at that moment. Images are composed of an array of pixels (picture elements). The 3D reality can be represented in many different ways, each with its own advantages and disadvantages. There are several examples of such **3D shape representations**, including depth images, point clouds, voxel grids, and meshes. **Depth images** contain distance information between the object and the camera at every pixel. The distance encodes 3D geometry information from a fixed point of view. Layered depth images (LDIs) use several layers of depth maps and

their associated color values to depict a scene. **Point clouds** comprise vertices in 3D space, represented by coordinates along the  $x$ ,  $y$ , and  $z$  axes. These types of data can be acquired by 3D scanners, such as LiDARs or RGB-D sensors, from one or more viewpoints. **Voxel grids** describe a scene or object using a regular grid in 3D space. A voxel (volume element) in 3D space is analogous to a pixel in a 2D image. A voxel grid can be created from a point cloud by voxelization, which groups all 3D points within a voxel. **Meshes** are a collection of vertices, edges, and polygonal faces. In contrast to a point cloud, which only provides vertices locations, a mesh also provides surface information of an object. Computer graphics applications commonly utilize meshes to represent 3D models. Nevertheless, deep learning does not provide a straightforward way to process surface information. Instead, many techniques resort to sampling points from the surfaces to create a point cloud from the mesh representation.

As shown in Fig. 1 (a), images can be obtained by rendering a 3D object or scene under certain viewpoints and lighting conditions. This forward process is called **rendering** (image synthesis). Rendering has been studied in computer graphics and a wide variety of renderers are available for use. The reverse process, **inverse rendering**, as shown in Fig. 1 (b), is to recover the underlying intrinsic components of objects or scenes from their rendered 2D images. These intrinsic components include shape (surface, depth, and normals), material (albedo, reflectivity and shininess), and lighting (direction, intensity). The information can be further used to render photorealistic images in different lighting conditions and camera positions. The inverse rendering papers [3], [4] are not classified as 3D-aware image synthesis methods in this survey as they are not deliberately designed for this purpose. The 3D-aware image synthesis methods in this survey include a similar inverse rendering process and a rendering process. In contrast, these methods typically do not produce explicit 3D representations such as meshes or voxels for rendering. They learn **neural 3D representations** (mostly implicit functions), render them into images with **differentiable neural rendering** technique, and optimize the network parameters by minimizing the difference between the observed and rendered images. We will discuss both neural implicit scene representations and differentiable neural rendering techniques in the following two sections.

### 2.2 Implicit Scene Representations

In computer vision and computer graphics, 3D shapes are traditionally represented as explicit representations like

depths, voxels, point clouds, or meshes. Recent methods propose to represent 3D scenes with neural implicit functions, such as occupancy field [5], signed distance field [6], and radiance field [7]. The implicit neural representation (INR, neural fields, or coordinate-based representation) is a novel way to parameterize signals across a wide range of domains. Taking images as an example, INR parameterizes an image as a continuous function that maps pixel coordinates to RGB colors. The implicit functions are often not analytically tractable and are hence approximated by neural networks. Here are some popular examples of INR.

### 2.2.1 Occupancy Field

Occupancy network [5], [8], [9] implicitly represents a 3D surface with the continuous decision boundary of a neural classifier. This function approximated with a neural network assigns to every location  $p \in \mathbb{R}^3$  an occupancy probability between 0 and 1. Given an observation (*e.g.*, image or point cloud)  $x \in \mathcal{X}$  and a location  $p \in \mathbb{R}^3$ , the representation can be simply parameterized by a neural network  $f_\theta$  that takes a pair  $(p, x)$  as input and outputs a real number which represents the probability of occupancy:  $f_\theta : \mathbb{R}^3 \times \mathcal{X} \rightarrow [0, 1]$ .

### 2.2.2 Signed Distance Field

Signed Distance Field [6] is a continuous function that models the distance from a queried location to the nearest point on a shape’s surface, whose sign indicates if this location is inside (negative) or outside (positive):  $SDF(x) = s, x \in \mathbb{R}^3, s \in \mathbb{R}$ . The underlying surface is implicitly described as the zero iso-surface decision boundaries of feed-forward networks  $SDF(\cdot) = 0$ . This implicit surface can be rendered by raycasting or rasterizing a mesh obtained through marching cubes [10].

### 2.2.3 Radiance Fields

Radiance Fields [7] (NeRF) have attracted growing attention due to its compelling results in novel view synthesis on complex scenes. It leverages an MLP network to approximate the radiance fields of static 3D scenes and uses the classic volume rendering technique [11] to estimate the color of each pixel. This function takes as input a 3D location  $x$  and 2D viewing direction  $d$ , and outputs an directional emitted RGB color  $c$  and volume density  $\sigma$ :  $f_\theta : (x, d) \rightarrow (c, \sigma)$ . It captures 3D geometric details based on pure 2D supervision by learning the reconstruction of given views.

There also exist many other implicit functions proposed to represent a scene, such as neural sparse voxel fields [12], or neural volumes [13].

## 2.3 Differentiable Neural Rendering

3D rendering is a function that outputs a 2D image from a 3D scene. Differentiable rendering provides a differentiable rendering function, that is, it computes the derivatives of that function in response to different parameters of the scene. Once a renderer is differentiable, it can be integrated into the optimization of neural networks. One use case for differentiable rendering is to compute a loss in rendered image space and back propagation can be applied to train the network. Driven by the prevalence of NeRF-based methods [7], volume rendering [11] becomes the most commonly

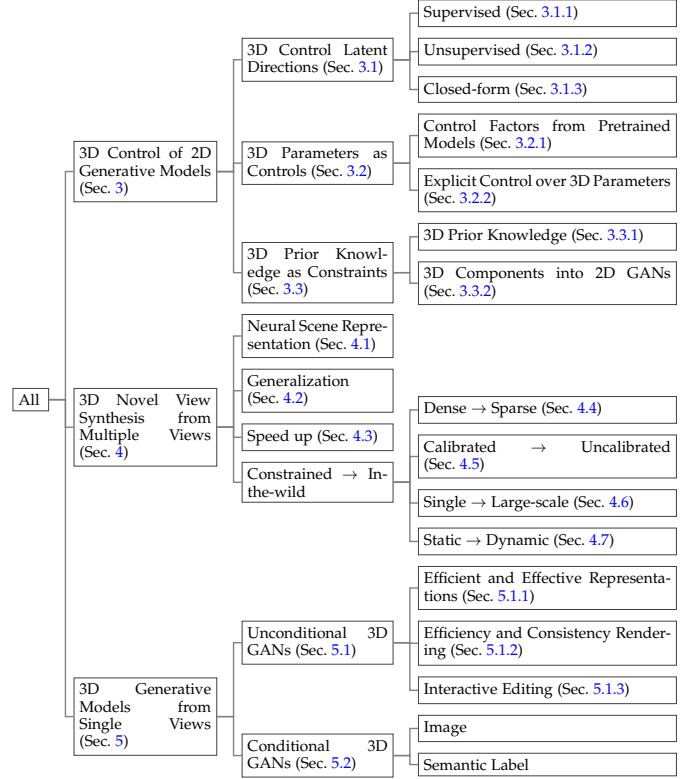


Fig. 2. A systematic taxonomy proposed in this survey of 3D-aware image synthesis methods.

used differentiable renderer among the methods that this survey targets. It is naturally differentiable, and the only input required to optimize the NeRF representation is a set of images with known camera poses. In [7], given volume density and color functions, volume rendering is used to obtain the color  $C(\mathbf{r})$  of any camera ray  $\mathbf{r}(t) = \mathbf{o} + t\mathbf{d}$ , with camera position  $\mathbf{o}$  and viewing direction  $\mathbf{d}$  using

$$C(\mathbf{r}) = \int_{t_1}^{t_2} T(t) \cdot \sigma(\mathbf{r}(t)) \cdot \mathbf{c}(\mathbf{r}(t), \mathbf{d}) \cdot dt, \quad (1)$$

where

$$T(t) = \exp\left(-\int_{t_1}^t \sigma(\mathbf{r}(s)) ds\right). \quad (2)$$

$T(t)$  denotes the accumulated transmittance, representing the probability that the ray travels from  $t_1$  to  $t$  without being intercepted. The rendered image can be obtained by tracing the camera rays  $C(\mathbf{r})$  through each pixel of the to-be-synthesized image.

## 2.4 Dataset

Based on the experimental setting and applicable scenarios, different categories of target papers use either multiple views or single views of the image collections. Multiple-view image datasets contain images of a scene taken from different viewpoints and are usually used in novel view synthesis methods (see Sec. 4). Similar to 2D models, 3D-aware generative models (see Sec. 5) aim to produce photo-realistic and multi-view consistent images. Therefore, the same single-view image datasets are used as in the 2D methods.

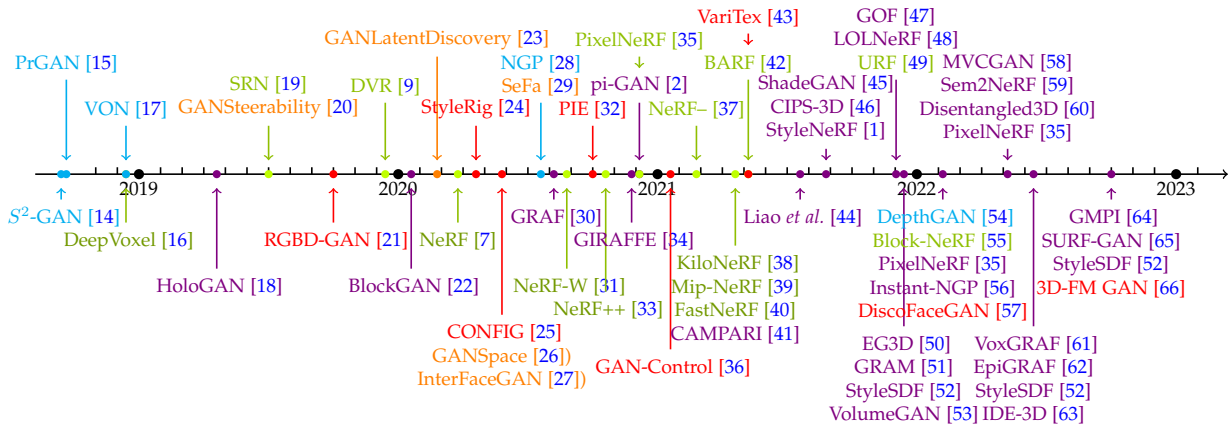


Fig. 3. Chronological overview of representative 3D-aware image synthesis methods which are categorized by different learning approaches. Methods in orange, red, cyan, lime, and violet are from Sec. 3.1, Sec. 3.2, Sec. 3.3, Sec. 4, and Sec. 5, respectively.  $S^2$ -GAN [14] and PrGAN [15] are published in 2016 and are not shown in scale. Best viewed in color.

### 2.4.1 Multiple-view image collections

Per-scene multiple-view image collections are usually used in the novel view synthesis methods. These methods aim to learn effective and expressive 3D representations and render novel view images or produce free-viewpoint videos from a collection of multiple-view images. Tab. 1 shows some example of multi-view image datasets. In early studies, input data must meet several strong assumptions, including diverse camera views, precise intrinsic and extrinsic camera parameters, and constant lighting conditions. Therefore, most of them either use synthetic data rendered from 3D scans or real images captured from real world, along with corresponding camera parameters and scene bounds. For synthetic data, they use ground-truth camera poses, intrinsics, and bounds; for real data, they use the off-the-shelf softwares (e.g. a structure-from-motion package COLMAP [74]) to estimate these parameters. Typically, it requires sufficient camera diversity and coverage over repeated observations of a target object or scene. An example of synthetic data rendering process is to center a scan (e.g., objects from ScanNet [75], ShapeNet [76], or DeepVoxels [16]) at the origin, scale it to lie within the unit cube, and render images at sampled viewpoints. The training set can be obtained by rendering the object from a number of poses uniformly distributed on the northern (upper) hemisphere while the test set obtained by rendering views on an Archimedean spiral. The most popular datasets in this setting are the LLFF [77] and NeRF [7] dataset, the DTU dataset [67], as well as the Tanks and Temples dataset [78].

As recent methods have attempted to reduce the constraints on the input data, the datasets are developed 1) from single objects to large-scale scenes and 2) from a constrained environment to in-the-wild real world. For example, the crowded Phototourism dataset [72] is widely used to perform view synthesis [73] as the unconstrained photo collections. The same object’s color may vary from image to image due to variable illumination and post-processing. For training without known camera parameters, NeRF++ [37] introduces a high-quality path-traced synthetic Blender Forward Facing (BLEFF) dataset to benchmark camera

parameter estimation and novel view synthesis quality. The San Francisco Alamo Square Dataset in Block-NeRF [55] covers an area of approximately 570 meters  $\times$  960 meters and contains millions of images with differing scene geometry (e.g., parked cars and construction work) and appearance (e.g., weather conditions and time of day).

### 2.4.2 Single-view image collections

Single-view image collections contain unstructured and unannotated single images, which are typically used by unconditional methods and some of the conditional methods. Current popular datasets include FFHQ [79], AFHQ [80], MetFaces [81], CompCars [70], and LSUN objects or scenes [82]. The single-view image collections can be further categorised into single objects [70], [79], [80], [81], [82] and multiple objects [83] according to the salient object numbers in the foreground, variable-shape [62] and simple shape [70], [79], [80], [81], [82] according to the fineness of the object. Tab. 2 demonstrates a summary of some single-view image datasets organized by their major categories and roughly sorted by their popularity how often they are used in studies).

**CelebFaces Attributes (CelebA)** [84] is a large-scale face attribute dataset consisting of 200K celebrity images with 40 attribute annotations each. CelebA, together with its succeeding CelebA-HQ [85], are widely used in face image generation and manipulation.

**Flickr-Faces-HQ (FFHQ)** [79] is a high-quality image dataset of human faces crawled from Flickr, which consists of 70,000 high-quality human face images of  $1024 \times 1024$  pixels and contains considerable variation in terms of age, ethnicity, and image background.

**Animal FacesHQ (AFHQ)** [79] consists of 70,000 high-quality animal face images of  $512 \times 512$  pixels. The dataset includes three domains of cat, dog, and wildlife, each providing 5,000 images and containing diverse images of various breeds ( $\geq$  eight).

**CARLA** [86] is a synthetic dataset, which contains 10K images which are rendered from Carla Driving simulator [86] using 16 car models with different textures.

TABLE 1  
Examples of multi-view image datasets.

| dataset              | published in | # scene               | # samples per scene | range (m <sup>2</sup> ) | resolution          | used in    | keyword                 |
|----------------------|--------------|-----------------------|---------------------|-------------------------|---------------------|------------|-------------------------|
| DeepVoxels [16]      | CVPR 2019    | 4 simple objects      | 479 / 1,000         | \                       | 512 × 512           | [7]        | synthetic, 360 degree   |
| NeRF Synthetics [7]  | ECCV 2020    | 8 complex objects     | 100 / 200           | \                       | 800 × 800           | [7], [39]  | synthetic, 360 degree   |
| NeRF Captured [7]    | ECCV 2020    | 8 complex scenes      | 20-62               | a few                   | 1,008 × 756         | [7]        | real, forward-facing    |
| DTU [67]             | CVPR 2014    | 124 scenes            | 49 or 64            | a few to thousand       | 1,600 × 1,200       | [68], [69] | often used in few-views |
| Tanks & Temples [70] | CVPR 2015    | 14 objects and scenes | 4,395 - 21,871      | dozen to thousand       | 8-megapixel         | [71]       | real, large-scale       |
| Phototourism [72]    | IJCV 2021    | 6 landmarks           | 763-2,000           | dozen to thousand       | 564-1,417 megapixel | [73]       | varying illumination    |
| Alamo Square [55]    | CVPR 2022    | San Francisco         | 2,818,745           | 570 × 960               | 1,200 × 900         | [55]       | real, large-scale       |

LSUN [82] contains approximately one million labeled images for each of 10 scene categories (*e.g.*, bedroom, church, or tower) and 20 object classes (*e.g.*, bird, cat, or bus). The church and bedroom scene images and car and bird object images are commonly used.

**Megascans Food** (M-Food) and **Megascans Plants** (M-Plants) [62] are two recently proposed *variable-shape* datasets. They are proposed to address two limitations of existing simple-shape benchmarks: 1) they contain low variability of global object geometry, focusing entirely on a single class of objects, like human/cat faces or cars, that do not vary much from instance to instance; 2) they have limited camera pose distribution: for example, FFHQ and Cats are completely dominated by the frontal and near-frontal views. M-Food consists of 199 models of different food items with 128 views per model (25,472 images in total); and M-Plants consists of 1,108 different plant models with 128 views per model (141,824 images in total). Both contain images with  $256 \times 256$  pixels.

**CLEVR $n$**  [22], [83] is a synthetic multiple-object dataset, where  $n$  is the number of foreground objects. This dataset is derived from CLEVR [83] in [22] by adding a larger variety of colours and primitive shapes. They use the render script from CLEVR [83] to randomly place foreground objects into the scene and render them. In response to demand, the image can be rendered to a desired quantity (*e.g.* 100k) and resolution (*e.g.*  $64 \times 64$  in [22] and  $256 \times 256$  in [34]). The CLEVR scene setups can be used to generate other synthetic datasets, including SYNTH-CAR $n$  and SYNTH-CHAIR $n$  with  $n$  foreground objects each. These include a fixed, grey background, a virtual camera with fixed parameters but random location jittering, and random lighting. These multiple-object datasets are used to test models in terms of the independent control over foreground and background [22], [34].

## 2.5 Evaluation Metrics

There are different dimensions to evaluate 3D-aware image synthesis methods, which can be categorized into two groups: 2D and 3D metrics. 2D metrics evaluate the synthesised images in terms of quality, diversity, and fidelity. 3D metrics access the shape and surface quality, as well as the temporal and multi-view consistency. Model efficiency is taken into account sometimes and is evaluated by model size and training/inference time.

### 2.5.1 Model Efficiency

Current methods use two metrics to show the efficiency of their proposed methods: average running time and model

complexity. Such metrics can be borrowed from deep compression, which evaluates inference runtime, model size and latency. The model complexity is typically assessed by the number of parameters, floating point operations (FLOPs), and multiply-accumulate operations (MACs). Runtime usually means one forward at inference phase. In our case, inference runtime means the time required for rendering an image. But for 3D image synthesis, we also care about the time required for training, which could be evaluated by total training time and batches per second [46].

### 2.5.2 Image Quality and Diversity

These metrics are often used to assess images generated by a generative model, like a generative adversarial network (GAN), mostly in Sec. 3.2 and Sec. 5. These metrics include but are not limited to Inception Score (IS) [87], Fréchet Inception Distance (FID) [88], Kernel Inception Distance (KID) [89], and Learned Perceptual Image Patch Similarity (LPIPS) [90].

**IS** is a widely used metric to measure the quality and diversity of images generated from GAN models. It calculates the statistics of a synthesized image using Inception-v3 Network [91] pretrained on ImageNet [92]. A higher score is better.

**FID** is defined by the Fréchet distance between feature vectors from the real and generated images based on the Inception-v3 [91] pool3 layer. Lower FID indicates better perceptual quality.

**KID** measures the dissimilarity between two probability distributions using samples drawn independently from each distribution. Lower is better.

**LPIPS** measures image perceptual quality using a VGG model [93] pretrained on ImageNet. A lower value means higher similarity between image patches.

### 2.5.3 Image Fidelity

Fidelity (or faithfulness) measures the similarity between the real image and the generated one. It can be approximated by the image similarity. When the groundtruth images exist at certain viewpoints, the rerendered images are expected to be close to them. The most widely used metrics of image fidelity are Peak Signal-to-Noise Ratio (PSNR) and Structural Similarity (SSIM) [94]. Some methods use the pixel-wise reconstruction distance, *e.g.*, mean absolute error (MAE), mean squared error (MSE), or root mean squared error (RMSE).

**PSNR** between the ground-truth image and the reconstruction is defined by the maximum possible pixel value of the image and the mean squared error between images.

TABLE 2  
Summary of popular single-view image datasets organized by their major categories and sorted by their popularity.

| dataset          | published in | category               | # samples | resolution  | representative references   | keyword                |
|------------------|--------------|------------------------|-----------|-------------|-----------------------------|------------------------|
| FFHQ [79]        | CVPR 2019    | Human Face             | 70k       | 1024 × 1024 | [1], [50], [52], [53]       | single simple-shape    |
| AFHQ [80]        | CVPR 2020    | Cat, Dog, and Wildlife | 15k       | 512 × 512   | [1], [50], [52], [53]       | single simple-shape    |
| CompCars [70]    | CVPR 2015    | Real Car               | 136K      | 256 × 256   | [1], [18], [22], [53]       | single simple-shape    |
| CARLA [86]       | CoRL 2017    | Synthetic Car          | 10k       | 128 × 128   | [2], [51], [53], [60], [69] | single simple-shape    |
| CLEVR $\pi$ [83] | CVPR 2017    | Objects                | 100k      | 256 × 256   | [22], [34]                  | multiple, simple-shape |
| LSUN [82]        | 2015         | Bedroom                | 300K      | 256 × 256   | [18], [53]                  | single, simple-shape   |
| CelebA [84]      | ICCV 2015    | Human Face             | 200k      | 178 × 218   | [18], [53]                  | single simple-shape    |
| CelebA-HQ [85]   | ICLR 2018    | Human Face             | 30k       | 1024 × 1024 | [48]                        | single, simple-shape   |
| MetFaces [81]    | NeurIPS 2020 | Art Face               | 1336      | 1024 × 1024 | [1]                         | single, simple-shape   |
| M-Plants [62]    | NeurIPS 2022 | Variable-Shape         | 141,824   | 256 × 256   | [62]                        | single, variable-shape |
| M-Food [62]      | NeurIPS 2022 | Variable-Shape         | 25,472    | 256 × 256   | [62]                        | single, variable-shape |

**SSIM** measures the structural similarity between images based on independent comparisons in terms of luminance, contrast, and structures. The details of these terms can be found in [94].

#### 2.5.4 Multi-view 3D Consistency

Multi-view 3D consistency is another significantly important aspect in 3D-aware image synthesis. The view-inconsistencies could be caused by shapes and colors. The consistency in photometry and geometry is basically equivalent to the quality of shape (surface) and texture (color).

**Shape Quality** is evaluated in most methods by calculating the differences between the rendered depth map and the pseudo-ground-truth depth, *e.g.* using MSE [50] or a modified Chamfer distance [52]. For example, given two generated images from two sampled angles of the same scene, Shi *et al.* [54] uses rotation precision and rotation consistency to evaluate the quality of the depth maps (point cloud). The former is aimed to measure the accuracy of the angle of rotation while the latter targets at the rotation consistency evaluation. In GOF [47], the mean angle deviation (MAD) and the scale-invariant depth error (SIDE) are used to compare the outputs against the ground-truth depth maps. MAD emphasizes the compactness of surfaces, whereas SIDE emphasizes the accuracy of depths. Some methods use more direct indicators to evaluate the geometry properties of learned surfaces. Xu *et al.* [47] uses average geodesic distance and average curvature between random points to assess the geometry properties of learned surfaces. The lower these two metrics, the smoother the recovered object surfaces.

**Texture Quality** could be evaluated by using PSNR and SSIM as image fidelity under different viewpoints. But in most cases, the ground-truth images are not available for evaluation. Several methods use FID to evaluate image quality at different camera poses as part of the multi-view texture quality. A more direct way is to assess multi-view facial identity consistency (ID) [50] by calculating the mean Arcface [95] cosine similarity score between pairs of views of the same synthesized face rendered from random camera poses.

Apart from the aforementioned performance measures, pose accuracy [50] is also considered as an important indicator of shape quality and controllability. Poses (pitch, yaw, and roll) are detected with the help of pre-trained face reconstruction models from the generated images and then

its L2 errors against the ground-truth poses is computed to determine each model’s pose drift. In the following sections, we introduce different kinds of 3D-aware image synthesis methods. The first (arXiv) draft dates are used to sequence the publications. The publication information can be found in the bibliography. Tab. 3 is a detailed comparison of 3D-aware image synthesis methods.

### 3 3D CONTROL OF 2D GENERATIVE MODELS

Due to their prevalence, there is a track of works aiming at to make 2D generative models, like GANs, especially StyleGANs [79], [81], [103], [104], 3D aware. These works, mostly built on the top of a pretrained StyleGAN, can be further categorized into three groups based on how the 3D control capability is introduced: 1) discovering 3D control latent directions, 2) adopting explicit control over the 3D parameters, and 3) introducing 3D-aware components into 2D GANs. Fig. 4 is an illustration of these three categories of methods.

#### 3.1 Discovering 3D Control Latent Directions

It has been demonstrated that pretrained GANs have interpretable directions in their latent spaces. The image generation process is controlled by altering the latent codes  $\mathbf{z}$  in the desired directions  $\mathbf{n}$  with step  $\alpha$ , which is often considered as a linear vector arithmetic  $\mathbf{z}' = \mathbf{z} + \alpha\mathbf{n}$ . The altered latent codes are then fed into a pretrained GAN  $G(\cdot)$  for the edited results:  $I' = G(\mathbf{z}')$ . Most approaches in this group are developed to edit semantic attributes. Besides semantic information, some methods have shown to be able to discover geometric directions in the pretrained GAN latent space. They are used to alter pose position or light condition of faces [27] or manipulate geometry (*e.g.*, zoom, shift, rotation) of natural images [23]. As classified in [105], such directions can be identified through supervised, unsupervised, or self-supervised manners. Recent methods [29], [106] have shown that latent directions for 3D-aware image synthesis can be directly computed in a closed form without any kind of training or optimization.

##### 3.1.1 Supervised Manner

Existing supervised learning-based approaches typically randomly sample a large amount of latent codes, synthesize a collection of corresponding images, and annotate them with some predefined labels by introducing a pretrained classifier [27], [107]. To control the head pose, they typically

TABLE 3

Overview of 3D-controllable image generation. *Condition* means the input besides noise vectors, such as images, 3D control parameters from other models, or viewpoints (some methods [15] get the camera poses or viewpoints also from noise vectors). The term location and view represent the 3D location (world coordinate)  $x = (x, y, z)$  and the 2D viewing direction  $(\theta, \phi)$ . *Dataset* means what kinds of images these methods used for training. Those trained on single-view imagery usually only supports a single image *Category*. For multiple-view imagery, these images can be densely or sparsely sampled (captured) multiple views of a scene, bounded or unbounded, static or dynamic. *Posed images* mean 2D images along with their respective extrinsic and intrinsic camera matrices. *Geometry* indicates if the model is available for geometry reconstruction. *Editability* means if the model has the ability of attribute edit beyond camera pose.

| Method   | Publication  | Dataset / Category              | Condition                  | Geometry | Editability | Supervision                 | Highlight                      |
|--|--------------|---------------------------------|----------------------------|----------|-------------|-----------------------------|--------------------------------|
| <b>3D Latent Control Directions</b>                      |              |                                 |                            |          |             |                             |                                |
| GANSteerability [20]                                     | ICLR 2020    | ImageNet                        | N/A                        | X        | ✓           | shifted image               |                                |
| GANLatentDiscovery [23]                                  | ICML 2020    | face, ILSVRC                    | N/A                        | X        | ✓           | unsupervised                |                                |
| InterFaceGAN [27]  | CVPR 2020    | face                            | N/A                        | X        | ✓           | synthetic image & label     |                                |
| GANSpace [26]  | NeurIPS 2020 | face, ImageNet                  | N/A                        | X        | ✓           | unsupervised                |                                |
| SeFa [29]  | CVPR 2021    | face, car, LSUN, ImageNet       | N/A                        | X        | ✓           | closed-form                 |                                |
| <b>3D Parameters as Controls</b>                         |              |                                 |                            |          |             |                             |                                |
| StyleRig [24]  | CVPR 2020    | face                            | GAN-generated image        | X        | ✓           | 3DMM                        |                                |
| DiscoFaceGAN [57]  | CVPR 2020    | face                            | parameters                 | X        | ✓           | 3DMM                        |                                |
| PIE [32]   | TOG 2020     | face                            | real image                 | X        | ✓           | 3DMM                        |                                |
| CONFIG [25]  | ECCV 2020    | face                            | real image / parameters    | X        | ✓           | synthetic data              |                                |
| GAN-Control [36]   | ICCV 2021    | face                            | parameters                 | X        | ✓           | pseudo param.               |                                |
| 3D-FM GAN [66]   | ECCV 2022    | face                            | real image and rendering   | X        | ✓           | synthetic data              |                                |
| <b>3D Priors as Constraints</b>                          |              |                                 |                            |          |             |                             |                                |
| S <sup>2</sup> -GAN [14]                                 | ECCV 2016    | scene (NYUv2)                   | unconditional              | X        | X           | normal map                  |                                |
| P <sub>r</sub> GANs [15]                                 | 3DV 2017     | synthesized from 3D shapes      | unconditional              | ✓        | X           | image and viewpoint         |                                |
| VON [17]   | NeurIPS 2018 | chair, car                      | unconditional              | ✓        | X           | 2.5D sketch, 3D shape       |                                |
| RCBD-GAN [21]  | ICLR 2020    | face, car                       | camera parameters          | ✓(depth) | X           | unsupervised                |                                |
| NGP [28]   | CGF 2021     | chair, car                      | user controls              | ✓        | ✓           | 3D shape, reflectance map   |                                |
| LiftedGAN [96]   | CVPR 2021    | face                            | unconditional              | ✓        | ✓           | pseudo multi-view images    |                                |
| DepthGAN [54]  | ECCV 2022    | scene (LSUN)                    | viewpoint                  | ✓(depth) | ✓           | pseudo depth map            |                                |
| <b>3D Novel View Synthesis (from multi-view imagery)</b> |              |                                 |                            |          |             |                             |                                |
| DeepVoxels [16]  | CVPR 2019    | dense bounded static scene      | view, image                | X        | X           | multi-view posed images     |                                |
| SRN [19]   | NeurIPS 2019 | dense bounded static scene      | view, location             | ✓        | ✓           | multi-view posed images     |                                |
| DVR [9]  | CVPR 2020    | dense bounded static scene      | view, location             | ✓        | X           | multi-view posed images     |                                |
| NeRF [7]   | ECCV 2020    | dense bounded static scene      | view, location             | X        | X           | multi-view posed images     |                                |
| NeRF++ [33]  | 2020         | dense unbounded static scene    | view, location             | X        | X           | multi-view posed images     |                                |
| NeRF-W [31]  | CVPR 2021    | dense bounded static scene      | view, location             | X        | X           | unconstrained posed images  |                                |
| PixelNeRF [35]   | CVPR 2021    | sparse bounded static scene     | view, location             | X        | X           | one or a few posed images   |                                |
| FastNeRF [40]  | CVPR 2021    | dense bounded static scene      | view, location             | X        | X           | multi-view posed images     |                                |
| KiloNeRF [38]  | CVPR 2021    | dense bounded static scene      | view, location             | X        | X           | multi-view posed images     |                                |
| D-NeRF [97]  | CVPR 2021    | dynamic scene                   | view, location             | X        | X           | multi-view posed images     |                                |
| Nerfies [98]   | CVPR 2021    | dynamic scene                   | view, location             | X        | X           | multi-view posed images     |                                |
| BARF [42]  | ICCV 2021    | dense bounded static scene      | view, location             | X        | X           | multi-view unposed images   |                                |
| Mip-NeRF [39]  | ICCV 2021    | dense bounded static scene      | view, location             | X        | X           | multi-view posed images     |                                |
| NeRF— [37]   | 2021         | dense front-facing static scene | view, location             | X        | X           | unposed front-facing images |                                |
| LFN [99]   | NeurIPS 2022 | dense bounded static scene      | image, pose                | X        | X           | multi-view posed images     | light field                    |
| Block-NeRF [55]  | CVPR 2022    | large-scale scene               | view, location             | X        | X           | unconstrained posed images  |                                |
| URF [49]   | CVPR 2022    | large-scale scene               | view, location             | X        | X           | unconstrained posed images  |                                |
| SRT [100]  | CVPR 2022    | dense bounded static scene      | image, (pose)              | X        | X           | posed or unposed images     | set-latent representation      |
| Instant-NeRF [56]  | TOG 2022     | dense bounded static scene      | view, location             | X        | X           | multi-view posed images     |                                |
| BungeeNeRF [101]   | ECCV 2022    | large-scale scene               | view, location             | X        | X           | unconstrained posed images  |                                |
| 3DiM [102]   | 2022         | dense bounded static scene      | image, pose                | X        | X           | posed images                | diffusion model                |
| <b>3D Generative Models (from single-view imagery)</b>   |              |                                 |                            |          |             |                             |                                |
| HoloGAN [18]   | ICCV 2019    | face, cat, car, LSUN            | camera pose                | ✓        | X           | unsupervised                | deep voxel                     |
| Liao <i>et al.</i> [44]                                  | CVPR 2020    | multiple object data            | unconditional              | X        | X           | unsupervised                | 3D primitives                  |
| BlockGAN [22]  | NeurIPS 2020 | multiple object data            | camera pose                | X        | ✓           | unsupervised                | deep voxel                     |
| GRAF [30]  | NeurIPS 2020 | rendered chair, face, cat, bird | camera matrix, pose        | X        | X           | unsupervised                | NeRF                           |
| pi-GAN [2]   | CVPR 2021    | face, car, CARLA                | camera position            | ✓        | X           | unsupervised                | NeRF                           |
| GIRAFFE [34]   | CVPR 2021    | chair, cat, face, car, church   | camera pose                | ✓        | ✓           | unsupervised                | compositional NeRF             |
| GOF [47]   | NeurIPS 2021 | cat, car, face                  | 3D location, camera pose   | ✓        | X           | unsupervised                | generative occupancy fields    |
| ShadeGAN [45]  | NeurIPS 2021 | cat, face                       | 3D location, camera pose   | ✓        | X           | unsupervised                | light field                    |
| CAMPARI [41]   | 3DV 2021     | cat, car, face, chair           | camera pose                | X        | ✓           | unsupervised                | decomposed NeRF                |
| CIPS-3D [46]   | 2021         | face                            | 3D location                | X        | X           | unsupervised                | NeRF                           |
| StyleNeRF [1]  | ICLR 2022    | face, cat, car                  | camera pose                | ✓        | X           | unsupervised                | NeRF                           |
| GRAM [51]  | CVPR 2022    | cat, face, CARLA                | camera pose                | ✓        | X           | unsupervised                |                                |
| EG3D [50]  | CVPR 2022    | cat, face                       | camera parameters          | ✓        | X           | unsupervised                | tri-plane 3D representation    |
| VolumeGAN [53]   | CVPR 2022    | cat, car, face, bedroom, CARLA  | camera pose                | ✓        | X           | unsupervised                |                                |
| StyleSDF [52]  | CVPR 2022    | cat, face                       | camera pose                | ✓        | X           | unsupervised                | SDF                            |
| MVCGAN [58]  | CVPR 2022    | cat, face                       | camera pose                | X        | X           | unsupervised                | NeRF                           |
| LOLNeRF [48]   | CVPR 2022    | cat, face, car                  | camera pose                | ✓        | X           | unsupervised                | generative latent optimization |
| Disentangled3D [60]                                      | CVPR 2022    | cat, face, CARLA                | camera pose, 3D location   | X        | X           | unsupervised                |                                |
| Pix2NeRF [69]  | CVPR 2022    | face, CARLA, rendered image     | image                      | X        | X           | unsupervised                |                                |
| Sem2NeRF [59]  | ECCV 2022    | cat, face                       | semantic mask, camera pose | X        | X           | semantic mask and image     |                                |
| GMPI [64]  | ECCV 2022    | cat, face                       | camera pose                | ✓        | X           | unsupervised                |                                |
| SURF-GAN [65]  | ECCV 2022    | face                            | camera pose                | X        | X           | unsupervised                |                                |
| VoxGRAF [61]   | NeurIPS 2022 | cat, face, CARLA                | camera parameters          | ✓        | X           | unsupervised                | sparse voxel grid              |
| EpiGRAF [62]   | NeurIPS 2022 | cat, face, variable-shape       | camera pose                | ✓        | X           | unsupervised                | tri-plane 3D representation    |
| IDE-3D [63]  | TOG 2022     | face                            | camera pose                | ✓        | ✓           | semantic mask and image     | tri-plane 3D representation    |

use pitch and yaw provided by some state-of-the-art tools (e.g. Microsoft Face API in [107]). For example, to interpret the face representation learned by GANs, Shen *et al.* [27] (May 2020) employ some off-the-shelf classifiers to learn a hyperplane in the latent space serving as the separation boundary and predict semantic scores for synthesized images. Even though the boundary is searched by solving a bi-classification problem, it can produce continuous face pose changing by moving the latent code. Abdal *et al.* [107] (August 2020) learn a bidirectional mapping between the  $\mathcal{Z}$  space and the  $\mathcal{W}$  space by using continuous normal-

izing flows (CNF). Attribute information (including head poses) are injected into the CNF blocks for the desired results. However, such methods rely on the availability of attributes (typically obtained by a face classifier network), which might be difficult to obtain for new datasets and could require manual labeling effort. Some self-supervised methods [20], [108] learn these directions or transformations without any direct supervision. Sequence of target images are simply obtained by applying simple augmentations to the source image. They make slight modifications to each transformation by controlling the strength to an expected

degree:  $\text{edit}(G(\mathbf{z}), \alpha)$ . Specifically, image shifting is used for camera motion along vertical and horizontal axes, downsampling and central cropping for zooming in and out, and perspective transformation for rotation. Since such transformation usually leads to undefined regions in the new image, only visible regions are involved in loss calculation. With the inverted images  $G(\mathbf{z})$  and target edits  $\text{edit}(G(\mathbf{z}), \alpha)$ , Jahanian *et al.* [20] (July 2019) learn the direction  $\mathbf{n}$  as

$$\mathbf{n}^* = \arg \min_{\mathbf{n}} \mathbb{E}_{\mathbf{z}, \alpha} [\mathcal{L}(G(\mathbf{z} + \alpha \mathbf{n}), \text{edit}(G(\mathbf{z}), \alpha))], \quad (3)$$

where  $\mathcal{L}$  measures the distance between the generated image  $G(\mathbf{z} + \alpha \mathbf{n})$  after taking an  $\alpha$ -step in the latent direction and the target image  $\text{edit}(G(\mathbf{z}), \alpha)$ .

### 3.1.2 Unsupervised Manner

The supervised setting would introduce bias into the experiment since the sampled codes and synthesized images used as supervision are different in each sampling and may lead to different discoveries of interpretable directions [29]. It also severely restricts the range of directions that existing approaches can discover, especially when the labels are missing. Furthermore, the individual controls discovered by these methods are typically entangled, affecting multiple attributes, and are often non-local. Thus, some methods [23], [26] aim to discover interpretable directions in the latent space in an unsupervised manner, *i.e.*, without the requirement of paired data. For example, Härkönen *et al.* [26] (April 2020) create interpretable controls for image synthesis by identifying important latent directions based on PCA applied in the latent or feature space. The obtained principal components correspond to certain attributes, and the selective application of the principal components allows for the control of many image attributes. Some of their discovered directions support 3D operations such as rotation or zooming out. This method is considered as “unsupervised” since the directions can be discovered by PCA without using any labels. Manual intervention and supervision are still required to annotate these directions to the target operations and to which layers they should be applied to.

### 3.1.3 Closed-form Solution

Recent methods [29], [106] propose closed form solutions of latent directions from the pretrained models. In [29], Shen *et al.* (July 2020) propose a semantic factorization method based on the singular value decomposition of the weights of the first layer of a pretrained GAN. They observe that the semantic transformation of an image, usually denoted by moving the latent code toward a certain direction  $\mathbf{n}' = \mathbf{z} + \alpha \mathbf{n}$ , is actually determined by the latent direction  $\mathbf{n}$ , which is independent of the sampled code  $\mathbf{z}$ . A **Semantics Factorization (SeFa)** method is developed to discover the directions  $\mathbf{n}$  that can cause a significant change in the output image  $\Delta \mathbf{y}$ , *i.e.*,  $\Delta \mathbf{y} = \mathbf{y}' - \mathbf{y} = (\mathbf{A}(\mathbf{z} + \alpha \mathbf{n}) + \mathbf{b}) - (\mathbf{A}\mathbf{z} + \mathbf{b}) = \alpha \mathbf{A}\mathbf{n}$ , where  $\mathbf{A}$  and  $\mathbf{b}$  are respectively the weight and bias of certain layers in  $G$ . The obtained formula,  $\Delta \mathbf{y} = \alpha \mathbf{A}\mathbf{n}$ , suggests that the desired editing with direction  $\mathbf{n}$  can be achieved by adding the term  $\alpha \mathbf{A}\mathbf{n}$  onto the projected code and indicates that the weight parameter  $\mathbf{A}$  should contain the essential knowledge of image variations. The problem

of exploring the latent semantics can thus be formulated as an optimization problem:

$$\mathbf{n}^* = \arg \max_{\{\mathbf{n} \in \mathbb{R}^d: \mathbf{n}^T \mathbf{n} = 1\}} \|\mathbf{A}\mathbf{n}\|_2^2. \quad (4)$$

The eigenvectors of the matrix  $\mathbf{A}^T \mathbf{A}$  should be the desired directions  $\mathbf{n}^*$ , *i.e.*, a closed-form factorization of latent semantics in GANs. This method supports multiple 3D control operations such as car orientation, face and body pose, streetscape and bedroom viewpoint, zoom, and rotation on a variety of GANs.

## 3.2 Incorporating 3D Parameters as Controls

Methods using 3D parameters as control factors typically follow a paradigm described as  $x' = G(x, \theta)$ . Explicit control over the 3D parameters  $\theta$  gives the edited result  $x'$ . Here,  $\theta$  could be human-interpretable attribute descriptions or a set of parameters from 3D models. Sometimes, the given control factors are intuitively understandable, *e.g.*, (age: 20 years old), (head pose: pitch, yaw, roll), or using the environment map to represent light condition. Most methods in this category incorporate 3D pretrained model parameters into 2D image-based generative models for controllable 3D-aware synthesis. These methods propose solutions to translate controls of 3D face rendering models into GAN-generated processes. Taking face generation as an example, they usually integrate priors from a parametric 3D Morphable Model (3DMM) [109] as explicit control factors. Tab. 4 is an overview of methods that incorporate 3D parameters to a 2D generative model.

The models in this section, as well as those in the next, make use of additional 3D models. Their main difference is that the former uses 3D model parameters as input control factors while the latter uses them as supervision signals. There is another series of studies combining implicit 3D representation with 3DMM, either being trained with a reconstruction loss using annotated multi-view datasets [110] or directly imposing 3DMM conditions into 3D NeRF volume and being trained on unannotated single-view images [111]. We focus on leveraging 3D priors for image synthesis based on 2D generative models and will introduce other studies in the remaining sections.

### 3.2.1 Control Factors from Pretrained Models

Most methods use 3DMM parameters to provide explicit control. 3DMMs [109] is commonly used to represent faces, where faces are parameterized by head rotation  $\phi$  and translation  $\rho$ , identity geometry  $\alpha$ , expressions  $\beta$ , skin reflectance  $\delta$ , and scene illumination  $\gamma$ :

$$\theta = (\phi, \rho, \alpha, \delta, \beta, \gamma) \in \mathbb{R}^m. \quad (5)$$

The parametric nature of 3DMMs allows navigating and exploring the space of plausible faces, *e.g.*, in terms of head pose, scene lighting, or facial expression. Thus, synthetic images can be rendered based on different parameter configurations. In practice, these 3DMM parameters are first transformed before being used in the network [32], [57]. Besides 3DMM, parameters from some other state-of-the-art tools could also be used to provide 3D control factors. In [107], Microsoft Face API predicts pitch and

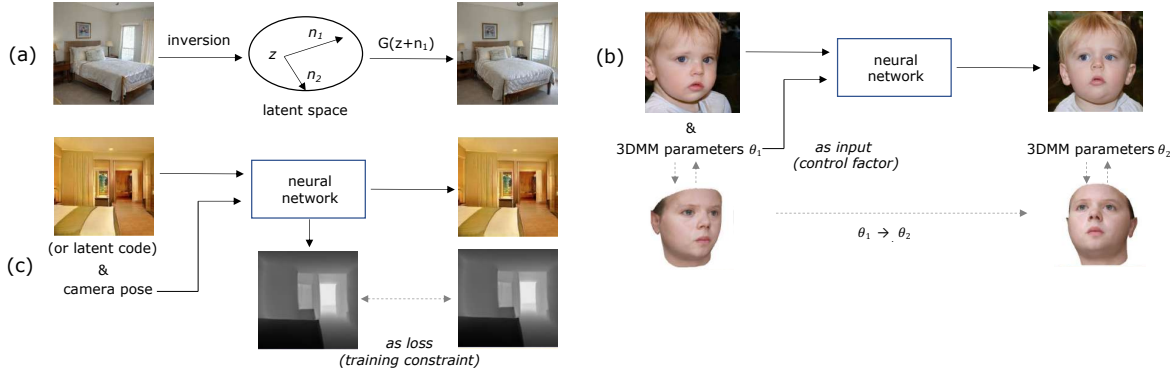


Fig. 4. Comparison of methods aiming to make 2D generative models (mostly GANs) 3D aware. These works are categorized into three groups based on how the 3D control capability is introduced: a) discovering 3D control latent directions in the pretrained GAN latent spaces, b) using 3D parameters (e.g. from 3DMM [109]) as input for explicit control, and c) introducing 3D-aware components (e.g. depth estimation module) into 2D GANs and adopting 3D prior knowledge (e.g. depth map) as training constraints.

yaw as the head pose. GAN-Control [36] extracts head-pose, expression, illumination, age, and hair color by using corresponding off-the-shelf attribute predictors. For example, they use head pose {Pitch, Yaw, Roll} represented as the Euler angles from [112]. DiscoFaceGAN [57] extracts identity, expression, and texture information from 3DMM, approximates scene illumination with Spherical Harmonics (SH) [113], and defines face pose as three rotation angles.

A key question is how to associate these parameters with corresponding images as these methods require supervised training. Except one using existing synthetic data with 3D parameters [25], others use pretrained models to achieve transformations from one direction to another, *i.e.*,  $I \rightarrow \theta$  by using attribute predictors [36] or  $\theta \rightarrow I$  by synthetic rendering [24], [66], and learn a mapping network for the opposite direction.

### 3.2.2 Explicit Control over 3D Parameters

With 3D parameters obtained, previous methods [24], [25], [32], [36], [66], [114] develop many different ways to incorporate them as input control into a 2D generative model for controllable 3D-aware image synthesis. Representative references in this group include CONFIG [25], MoFA [114], StyleRig [24], PIE [32], DiscoFaceGAN [57], GAN-Control [36], and 3D-FM GAN [66]. The following demonstrates how these methods introduce the parameters and achieve explicit controls by data collection, network design, and loss functions.

In MoFA [114], Tewari *et al.* (March 2017) use a CNN to project a face into the 3DMM space, followed by a differentiable renderer to synthesize the reconstructed face. The network is trained on a large collection of face images in a self-supervised manner. Following a computer graphics pipeline, CONFIG [25] (May 2020) uses a set of parameters to represent and control desired factors, such as head shape, facial hair style, facial expression, and illumination. Blendshapes with values in  $(0, 1)$  control facial expressions, Euler angles control head pose, and environment maps control the illumination. CONFIG has two encoders ( $E_R$  and  $E_S$ ) that encode real face images  $I_R$  and the parameters  $\theta : \{\theta_1, \dots, \theta_k\}$  of the synthetic images  $I_S$  to a shared latent space  $\mathcal{Z}$ , which is factorised into elements that each part  $z_i$  corresponds to a different facial attribute controlled by  $\theta_i$ . Swapping  $z_i$  of  $z \in \mathcal{Z}$  leads to semantically-

meaningful edits.  $z_i$  comes as the  $i$ -th parameter either from  $\theta_i$  (encoded by  $E_S$ ) or from a different real face image (encoded by  $E_R$ ). They adopt a two stage-training scheme to learn a disentangled latent space and produce photorealistic images.

Those based on StyleGANs [79], [81], [103] either use a pretrained StyleGAN model that keeps its weights fixed [24], [32] or make slight modifications to how 3D parameters are incorporated as conditions [36], [57]. StyleRig [24] and PIE [32] are two examples of using a pretrained StyleGAN. StyleRig (April 2020) trains a neural network, called RigNet, to inject a subset of parameters into a given StyleGAN latent code  $w$ . RigNet is a function  $\text{rignet}(\cdot, \cdot)$  that maps a pair of StyleGAN code  $w$  and subset of 3DMM parameters  $\theta$  to a new StyleGAN code  $w'$ , *i.e.*  $w' = \text{rignet}(w, \theta)$ . A number of RigNet models are trained, each dealing with a single mode of control (pose, expression, lighting). For self-supervised training, they introduce two key components: a learnable parameter regressor  $\mathcal{F}$  and a pretrained differentiable render layer  $\mathcal{R}$ .  $\mathcal{F}$  maps a latent code  $w$  to a vector of semantic control parameters  $\theta$ :  $\theta = \mathcal{F}(w)$ .  $\mathcal{R}$  takes a face parameter vector  $\theta$  as input and generates a synthetic rendering  $I_w = \mathcal{R}(\theta)$  of the face. RigNet is implemented as a linear two-layer perceptron (MLP).  $\mathcal{F}$  is a three layer MLP with ELU activations after every intermediate layer. StyleRig [24] allows for multiple-attribute editing but only on synthetic facial images rather than real ones. In contrast, PIE [32] (September 2020) uses a model-based face auto-encoder to replace  $\mathcal{F}$  and  $\mathcal{R}$  of StyleRig in support of real image editing.

Some methods inherit the main structure of Style-based generators and make slight modifications, mainly different on how the 3D parameters are incorporated as the condition. GAN-Control [36] (January 2021) builds on the StyleGAN2 [103] architecture. They divide the  $\mathcal{Z}$  and  $\mathcal{W}$  latent spaces to  $N + 1$  separate sub-spaces, in accordance with  $N$  control attributes and one residual one for non-concerned information. The original StyleGAN2 architecture is changed from a single mapping network ( $w = f(z)$ ), implemented as an eight-layered MLP to each control  $z_i$  having its own  $f(\cdot)$  so that  $w_i = f(z_i)$ . The combined latent vector (concatenation of the sub-vectors),  $w$ , is then fed into the generator  $G$ . To enable explicit control over each attribute, they use contrastive learning for disentanglement.

TABLE 4  
Overview of methods that incorporate 3D parameters to a 2D generative model.

| Method            | Publication | Control Factor                                  | Supervision ( $\theta \rightsquigarrow I$ ) |
|-------------------|-------------|---|---|
| StyleRig [24]     | CVPR 2020   | 3DMM parameters; $\theta$                       | $I = \mathcal{R}(\theta)$                   |
| DiscoFaceGAN [57] | CVPR 2020   | 3DMM, SH, angle vector; $\theta$                | $\theta = \mathcal{F}(I)$                   |
| PIE [32]          | TOG 2020    | 3DMM parameters; $\theta$                       | $\theta = \text{MoFa}(G(w))$                |
| CONFIG [25]       | ECCV 2020   | graphic parameters $\theta$                     | synthetic images with $\theta$              |
| GAN-Control [36]  | ICCV 2021   | instutive representation $y$                    | $y_i = \mathcal{R}_i(G(z))$                 |
| 3D-FM GAN [66]    | ECCV 2022   | a rendering $I_r(\theta)$ (equiv. to $\theta$ ) | (image, rendering) pairs                    |

Given a set of pretrained attribute predictors  $\{\mathcal{R}_i\}_{i=1}^N$ , they extract intermediate features as the attribute information from sampled images  $G(z)$  and use them to calculate the distances during training. To support explicit control during inference, they further train  $N$  encoders  $\{E_k\}_{k=1}^N$ , each to map a human-interpretable attribute representation  $y^k$  to a latent code  $w^k$ . They use the attribute predictors to label the randomly-sampled images as the training data. DiscoFaceGAN [57] (April 2020) proposes an unconditional 3D-aware method with controllability on four attributes: identity  $\alpha$ , expression  $\beta$ , scene illumination  $\gamma$ , and face pose  $\delta$ . Their model consists of two networks that learn the mapping 1)  $V(\cdot)$  from  $z$ -space to  $\theta$ -space; and 2)  $G(\cdot)$  from  $\theta$ -space to the image space. The latent code  $z$  is sampled from a standard normal distribution. The parameters  $\theta$  is the concatenation of the four control factors  $\theta := [\alpha, \beta, \gamma, \delta, \varepsilon]$  and the noise  $\varepsilon$ , which is the same of  $z$  for image diversity. They train four VAEs for  $\alpha$ ,  $\beta$ ,  $\gamma$ , and  $\delta$  on the  $\theta$  samples extracted by using a off-the-shelf 3D face reconstruction method from real image set. Only the decoders are kept after the VAE training and denoted as  $V_i, i = 1, 2, 3, 4$ , for  $z$ -space to  $\theta$ -space mapping. For training  $G$ , they sample  $z = [z_1, \dots, z_5]$  from standard normal distribution, map it to  $\theta$ , and feed  $\theta$  to both  $G$  and the renderer to obtain a generated face  $x$  and a rendered face  $x'$ , respectively. They apply three types of losses for training: adversarial loss, imitative loss, and contrastive loss. Different from GAN-Control [36], in 3D-FM GAN [66], Liu *et al.* (August 2022) change StyleGAN  $G$  to make it conditional on a given image and a rendering. They estimate the lighting and 3DMM parameters of the face as the 3D parameters  $\theta$ . These  $\theta$  are not directly incorporated into  $G$  as the explicit control signal but are used instead to generate a rendering  $I_r(\theta)$  of the same given image  $I(\theta)$ , which leads to a paired dataset. The resulting pairs  $\{I(\theta), I_r(\theta)\}$  are used for reconstruction training, and  $\{I(\theta_i), I_r(\theta_j)\}$  with different attributes of the same identity are for disentangled training.

### 3.3 Introducing 3D prior knowledge as Constraints

Both Sec. 3.2 and this section aim to make a 2D generative model, especially GAN, 3D-aware. Sec. 3.2 focuses on the methods that incorporate 3D prior knowledge to 2D GANs for explicit control, while this section emphasizes those methods that introduce 3D-aware components into 2D GANs and use 3D prior knowledge as constraints for training. In addition to whether to introduce explicit 3D parameters as inputs, the slight difference between them is also reflected in the different concepts of dataset usage and network structure design. The former is able to control each of the desired attributes because of introducing 3D parameters as control factors but it lacks explicit geometry and

texture as holistic 3D supervision, which leads to multi-view inconsistencies. The latter introduces 3D-aware components into 2D generative models (mostly GANs) and uses 3D prior knowledge (*e.g.* predicted depth from a off-the-shelf depth estimation method) to constrain the training process, resulting in a degree of consistency but in the meantime a lack of fine-grained control. The two types of methods are not mutually exclusive. In addition to introducing 3D parameters to improve controllability, a few methods also implement 3D constraints to improve consistency across multiple views. In particular, DiscoFaceGAN [57], PIE [32] and StyleRig [24] leverage 3DMM to establish losses to ensure 3D consistency based on a 2D image-based StyleGAN generator [79], [81], [103]. The representative studies discussed in this section include  $S^2$ -GAN [14], VON [17], NGP [28], DepthGAN [54], and LiftedGAN [96].

#### 3.3.1 3D Prior Knowledge

Some studies facilitate the learning of 3D consistency by utilizing one or more kinds of 3D prior knowledge as constraints, such as shape [17], [28], [115], albedo [96], [116], normal [116], and depth [21], [54], [96]. Basically, the intrinsic components used to describe the physical world can be used here as priors, including but not limited to shape (surface, depth, and normal), material (albedo, reflectivity and shininess), and lighting (direction, intensity). We introduce in Sec. 2.1 some common shape representations. Albedo, also referred to as reflection coefficient, is a measure of how reflective a surface is. It is either determined by a value between 0 and 1 or a percentage value. The more reflective a surface is, the higher the albedo value. A surface normal, or simply normal, to a surface at each point is a vector perpendicular to the tangent plane of the surface at that point. Normals represent the curvature of the object and can be used for reflecting light. Depth is the distance between the camera and the object at each pixel. They all contain geometric contextual features. There is a track of studies of intrinsic decomposition, which can be seen as a simplification of inverse rendering for general scenes, aiming to provide interpretable intermediate representations from images. There are also many methods specifically proposed to infer one specific environmental component, such as depth estimation, surface normal estimation, and light estimation. All these pretrained models can be potentially used as the training constraints for this category of methods.

#### 3.3.2 Introducing 3D-aware Components into 2D Generative Models

With the chosen 3D priors, the next important decision for this kind of methods is to find a way of introducing 3D-aware components and using 3D priors as constraints. In VON [17], Zhu *et al.* (December 2018) use shape as the 3D prior and design a GAN based on 3D convolutional neural network to learn the geometry information. An unconditional shape GAN  $G_s$  first generates voxel grid shape  $s$  from a randomly sampled shape code  $z_s$ . The differentiable projection module then projects  $s$  to 2.5D sketches  $s_{2.5D}$  at a sampled viewpoint  $z_v$ . The 2.5D sketches include both the object's depth and silhouette. The texture network  $G_t$  finally adds realistic, diverse texture to these

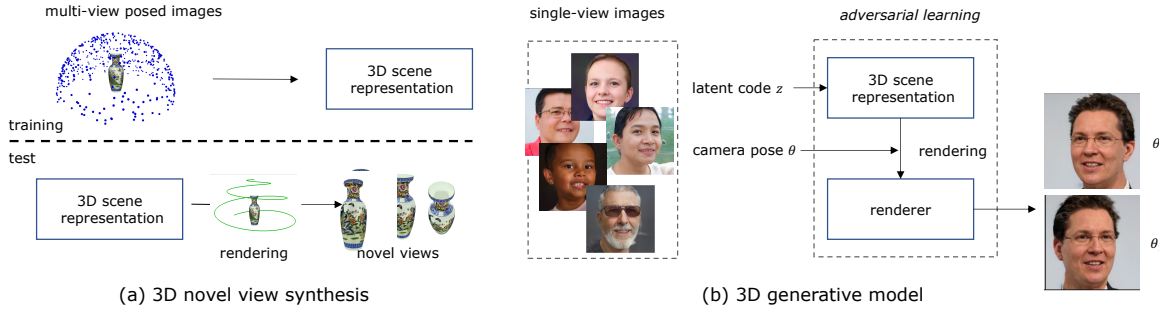


Fig. 5. The clarification of the defined terminology and the differences between 3D novel view synthesis methods (Sec. 4) and 3D generative models (Sec. 5). Both aim to generate multi-view-consistent and photo-realistic images, using a similar pipeline that first learns the 3D representation and then renders it from that viewpoint. It is their application scenarios and training data that differentiate the two kinds of methods. 3D novel view synthesis (a) learns a 3D representation from *multiple views* of a scene. As with their 2D counterparts, 3D generative models (b) learn to generate images from a collection of *single views*. The term *3D generative models* may also be used to refer to 3D novel view synthesis methods, but this survey uses this term only in reference to the methods trained on single view images.

2.5D sketches to generate 2D images:  $G_t$  takes  $s_{2.5D}$  and another latent code  $z_t$  as input and outputs a 2D images. NGP [28] (February 2021) and GIS [116] (September 2018) utilize more than one 3D prior, such as albedo maps and normal maps, resulting in multiple 2D GANs to learn all the 3D attributes.  $S^2$ -GAN [14] (March 2016) uses a two-stage training for indoor scene synthesis: an unconditional GAN for structure (geometry) generates a surface normal map and the second GAN for style (appearance) takes this surface normal map as condition and outputs an image. In the above methods, 3D-aware components are used as intermediates, which are supervised by outputs from pre-trained models. There are a few methods that only introduce 3D-aware components into 2D models without using 3D priors from pretrained models to constrain the training. For example, RGBD-GAN [21] (September 2019) generates two RGBD images with different camera parameters and then warps them to each other to ensure 3D consistency. This method learns to generate images consistent with the 3D world from pure 2D image collections.

More recently, a few methods, *e.g.* LiftedGAN [96] and DepthGAN [54], are build on top of StyleGAN architectures, either using a pretrained StyleGAN or adapting the vanilla design to their setting. They [54], [96] are also referred to as StyleGAN2-based 2.5D GANs in [50]. LiftedGAN [96] (November 2020) equips a pre-trained StyleGAN2 generator  $G_{2D}$  with five additional 3D-aware networks:  $D_V$ ,  $D_L$ ,  $D_S$ ,  $D_T$  and  $M$ , which respectively map a randomly sampled style code  $\hat{w}$  to the representation of viewpoint  $V$ , light condition  $L$ , depth  $S$ , transformation map  $T$ , and a neutralized  $\hat{w}_0$  at the default parameters of neutralized lighting  $L_0$  and viewpoint  $V_0$  (disentangle the latent space of StyleGAN2 into texture, shape, viewpoint, lighting). StyleGAN2  $G_{2D}$  outputs a face  $G_{2D}(w)$  serving as the proxy image and its neutralized face  $G_{2D}(w_0)$  as texture map. This neutralized face is then de-lighted by  $L_0$  under a Lambertian model to obtain the albedo map  $A$ . These 3D components are then used for rendering synthetic images, *i.e.* a differentiable renderer  $R$  is used to output a rendered image  $I_w = R(A, S, T, V, L)$ . For training, LiftedGAN uses multi-view images  $G_{2D}(w)$  from a pretrained StyleGAN as the supervision in a self-supervised manner, without the requirement of manually-annotated data nor 3DMM model parameters. The proposed model is able to output both the

3D shape and texture, allowing explicit pose and lighting control over generated images. To control the viewpoint, DepthGAN [54] (February 2022) designs a dual-generator based on StyleGAN. The depth branch  $G_d$  takes as the input an uniformly sampled angle  $\theta$  from range  $[\theta_l, \theta_r]$  and a depth latent code, and synthesize a depth image at  $\theta$ . The rgb branch  $G_r$  takes the intermediate feature maps of  $G_d$  as the conditions to acquire the geometry information. They use a pre-trained depth prediction model to get the corresponding depth image of each RGB image. A rotation consistency loss is introduced to enhance the multi-view consistency during training. The image synthesized under angle  $\theta_1$  is projected to a point cloud and re-projected to the 2D space under  $\theta_2$ , and compared with the image generated under  $\theta_2$ .

Despite their impressive image quality, these models still tend to produce 3D inconsistent faces under large expression and pose variations or scenes under different viewpoints due to the lack of a holistic 3D representation. These methods also inherit the inconsistencies introduced by the pretrained model they use. For example, depth estimation methods, especially depth estimated from a single image, are known to suffer from the world-inconsistency. With the advances in differentiable rendering and implicit neural 3D representations, a recent line of work has explored photo-realistic 3D-aware face or scene generation using *only* 2D image collections as the training data, *without any 3D supervision*. We introduce these kinds of work in the following two sections.

## 4 3D NOVEL VIEW SYNTHESIS

This section mainly introduces methods under the single-scene overfitting (SSO) experiment, which aims to render novel views by learning a deep neural scene representation from multi-view image collections of a scene or object. These models are trained per-scene and are proposed for the task of 3D reconstruction and either novel view synthesis or free viewpoint rendering. This corresponds to the three key components and improvement directions of recent algorithms: (better) deep 3D representation, (faster) rendering process, and (a smaller number of unlabeled and unstructured) training data (captured in a more real world environment). Methods introduced Sec. 5 are also inspired by those in this section. Fig. 5 illustrates the general pipeline of the two

kinds of methods. Both sections aim to infer a 3D scene representation from few images that can be used to render novel views. We categorize the related studies according to their underlying 3D representations (Sec. 4.1), as well as their efforts of new scene generalization (Sec. 4.2), training /inference acceleration (Sec. 4.3), and loose of constraints on the input data. The relaxation of constraints on input data expands the applicable scenario from a constrained environment to the real world, specifically 1) from a dense-view to a sparse-view image collection (Sec. 4.4); 2) from a calibrated to an uncalibrated image collection (Sec. 4.5); 3) from a single object to a large-scale scene (Sec. 4.6); and 4) from a static to a dynamic scene (Sec. 4.7). Tab. 5 is a comparison of 3D novel view synthesis methods using different 3D neural representations.

#### 4.1 Different Neural Scene Representations

To render real-world scenes, early methods follow a computer graphics framework, which requires a pre-defined explicit model. Following that are generative methods for rendering novel views by concatenating target poses with latent codes or directly transforming views within the latent space. These methods lead to inconsistent results under different viewpoints. Instead, recent works have explored neural implicit methods, following the basic idea of representing a scene as a continuous function that maps a spatial location to a feature representation of learned scene properties at that spatial location. Neural implicit shape representations offer many potential benefits over conventional discrete representations, including memory efficiency and a high spatial resolution. For example, DeepVoxels [16] (December 2018) is a learned representation that encodes the view-dependent appearance of a 3D scene without having to explicitly model its geometry. Scene Representation Networks (June 2019) [19] represent a scene implicitly as a continuous function that maps a 3D world coordinate to a feature-based representation of the scene properties at that coordinate:

$$\Phi : \mathbb{R}^3 \rightarrow \mathbb{R}^n, \quad \mathbf{x} \mapsto \Phi(\mathbf{x}) = \mathbf{v}. \quad (6)$$

It consists of a continuous, 3D-structure-aware neural scene representation and a renderer that efficiently encapsulate both scene geometry and appearance. It is trained in an end-to-end manner from posed 2D images without 3D supervision. Given a scene representation  $\Phi$ , a neural rendering maps  $\Phi$  with camera parameters to an image.

Most notably, Mildenhall *et al.* [7] (March 2020) propose Neural Radiance Fields (NeRF), which achieve photorealistic quality by implicitly modeling the volumetric density and directional emitted radiance of a scene. It represents a continuous scene as a 5D vector-valued function whose input is a 3D location  $x = (x, y, z)$  and a 2D viewing direction  $(\theta, \phi)$ , and whose output is an emitted color  $c = (r, g, b)$  and a volume density  $\sigma$ . The color of any ray passing through the scene is rendered using principles from classical volume rendering [11]. In NeRF, the rendering procedure samples a scene with one ray per pixel. This may result in excessive blurring or aliasing if the training or test images are observed at different resolutions. Moreover, the straightforward solution of rendering multiple rays

per pixel is impractical since each ray requires a hundred queries of the MLP. Mip-NeRF [39] (March 2021) is therefore proposed to use cone tracing instead of ray tracing of standard NeRF volume rendering. These representations encode a scene in the 3D space, which can be referred to as the *3D-structured neural scene representations*.

To handle the prohibitively expensive rendering process of the 3D-structured neural scene representations, some methods learn to represent a scene with a latent vector from which novel views can be synthesized. Light Field Networks (LFN) [99] (June 2021) uses an auto-decoder to infer a latent code from input images, which then conditions an MLP to compute radiance values for rays of novel views. The rendering of LFN only requires one query per pixel, as opposed to hundreds of times required for rendering 3D-structured neural scene representations such as SRN [19], NeRF [7], or DVR [9]. Their network design enables real-time rendering and vast reduction in memory consumption. Scene Representation Transformer (SRT) [100] (November 2021) proposes a set-latent scene representation, which is processed by an encoder transformer the patch features extracted from images. The decoder transformer queries this representation to generate the pixel color for a view ray. They are also referred to as the *geometry-free approaches* as they do not encode a scene in the 3D space as opposed to the aforementioned methods. Some (*i.e.*, CodeNeRF [117], NeRF-VAE [118]) combine such global latent scene representation with NeRF, leading to an advantage of generalization for the sparse input view setting.

The representations here mean those encode both appearance and geometry of the underlying 3D scenes. It is noteworthy that some related methods, such as occupancy networks [5], DeepSDF [6], or MetaSDF [119], are proposed for 3D shape reconstruction but model geometry only with no appearance information, meaning them not able to render images with photorealistic textures. Therefore, we do not categorize them as our target methods in this survey. But it would be beneficial to pay attention to those works as these representations can also be used for the 3D-aware image synthesis task. They can be introduced as the geometric representation along with a textural representation (*e.g.*, Texture Field [120]) for 3D image synthesis.

The vanilla NeRF [7] works for a single object or a small static scene, with the requirement of sufficient camera coverage and diversity over repeated observations of a target scene or object. In addition, the costly sampling and MLP queries in volume rendering make training and inference cumbersome. Several extensions have been proposed to mitigate some its shortcomings, including ones to be generalizable to new scenes [118], accelerate rendering [12], [38], [40], [121], [122], handle color variations [73], optimize camera poses [42], perform well with sparse or even few images [35], [68], [123], [124], and accommodate large-scale [49], [55], [101] or dynamic scenes [125]. Similar to the dominance of NeRF-based representations in Sec. 5, methods in this section are also mainly based on NeRFs and their variants. In Sec. 4.1, we have introduced methods based on different representations. The improvement strategies involved in the following sections are primarily based on NeRFs.

## 4.2 Generalizable to New Scenes

One drawback of NeRF is that the trained network (*i.e.*, a learned radiance field) can only represent a single structure, and thus is unable to generalize across novel geometries. Several NeRF extensions [35], [68], [117], [126], [127] have been proposed that do not require per-scene optimization on densely captured images. These methods rely on explicit 3D-to-2D projections of samples along the rays to gather features extracted from CNNs, which are then aggregated by a neural network for each point [35], [126], [127], or into a voxel grid [68]. In this way, these networks can be pre-trained, and then applied to novel scenes without optimization or additional per-scene fine-tuning. For example, in [127], Trevithick *et al.* propose a general radiance field (GRF) (October 2020). GRF consists of four components: 1) general feature extraction from the input images for every light ray; 2) feature reprojection to the query 3D point using multi-view geometry; 3) reprojected feature aggregation; 4) aggregated feature rendering of the query 3D point along a particular query viewpoint, and producing color and density via NeRF. PixelNeRF [35] (December 2020) proposes to condition a NeRF on image inputs, which allows the network to be trained across multiple scenes to learn a scene prior, enabling it to perform novel view synthesis in a feed-forward manner from a sparse set of views (as few as one). PixelNeRF can be trained on a set of multi-view images, allowing it to generate plausible novel view synthesis from very few input images without test-time optimization. IBNet [126] (February 2021) learns a generic view interpolation function that generalizes to novel scenes. MVNeRF [68] (March 2021) uses a deep 2D CNN to extract features of input images, warps each feature map to the reference view, and constructs the cost volume from the warped feature maps. The 3D CNN is applied to reconstruct a neural encoding volume with per-voxel neural features, which are then used to regress color and density. MVNeRF can generalize across scenes and generate photo-realistic novel view results given only three nearby input views. NeRF-VAE [118] (April 2021) uses a scene function, which is shared between scenes and conditioned on a per-scene latent code. The scene function contains shared information (*e.g.* available textures and shapes or properties of common elements), while the latent code contains scene-specific information (*e.g.* object position and category, lighting, or colour). NeRF-VAE is able to infer the structure of an unknown scene from very few input views. CodeNeRF [117] (September 2021) learns to disentangle shape and texture with separate geometry and appearance codes. During inference, given a single unposed image of an unseen object, CodeNeRF jointly optimizes the geometry and appearance codes, as well as the camera pose. Unseen objects can first be reconstructed from the given image and then rendered to a novel view. Aside from NeRF, there are some methods based on different representations that are with generalization capabilities, *e.g.* SRT [100] and LFN [99].

## 4.3 Speed-up Training and Inference

The original implementation of NeRF [7] uses hierarchical rendering to increase computation efficiency, but the sampling process and the densely evaluating MLPs at all query

points along each camera ray are still too time-consuming. Most attempts of subsequent works for acceleration can be broadly classified into two categories. The first category [38], [40], [121], [122], [128] trains, precomputes, and stores NeRF MLP evaluation results into more easily accessible data structures. This only increases inference speed. The second category [12], [56], [129], [130] usually jointly optimize a separate scene feature and a decoder MLP in a mutually beneficial manner, which can improve both training and inference speed. Typically, the efficiency and expressiveness of this learned scene feature support more efficient point sampling strategy.

In the first category, for example, SNeRG [128] (July 2020) stores precomputed diffused color, density, and feature vectors on a sparse voxel grid (referred to as baking in the paper). During evaluation, an MLP is used to produce specular color, which, combined with the specular colors alpha composited along the ray, produced the final pixel color. A concurrent work, PlenOctree (spherical harmonic NeRF, NeRF-SH) [121] (March 2021) predicts the spherical harmonic coefficients rather than the color function. The authors built an octree of precomputed spherical harmonic coefficients of the colors MLP. During the building of the octree, the scene was first voxelized, with low transmissivity voxels eliminated. FastNeRF [40] (March 2021) factorizes the color function into the inner product of the output of the direction position dependent MLP and the output of a direction-dependent MLP. This allows FastNeRF to easily cache color and density evaluation in a dense grid of the scene. KiloNeRF [38] (March 2021) separates the scene into thousands of cells, and trains independent MLPs for color and density predictions on each cell. These thousands of small MLPs are trained using knowledge distillation from a large pretrained teacher MLP.

In the second category, Neural Sparse Voxel Fields (NSVF) [12] (July 2020) models a scene as a set of radiance fields bounded by voxels. Feature representations are obtained by interpolating learnable features stored at voxel vertices, which are then processed by a shared MLP to compute color and density. NSVF uses sparse voxel intersection-based point sampling for rays. This strategy is much more efficient than dense or hierarchical sampling. Instant-NGP [56] (January 2022) greatly accelerates NeRF model training and inference. They propose a parametric multiresolution hash encoding that has been trained simultaneously with NeRF model MLPs. Further ray marching techniques are employed, such as exponential stepping, empty space skipping, and sample compaction. These techniques are also often used in other methods to further improve training and inference speed in conjunction.

In the following sections, we introduce the efforts of follow-up works to reduce the constraints on the input data from a constrained environment to in-the-wild real world.

## 4.4 From Dense to Sparse

The baseline NeRF requires per-scene optimization on densely captured images with known camera poses. It will suffer from overfitting to individual views and non-sensible scene geometry if there are not enough training samples, or the samples are not varied enough in pose. This

makes it impractical as it requires a large number of posed images and a lengthy per-scene optimization. A family of methods [35], [68], [123], [124] propose data-efficient NeRF models for reconstructing radiance fields from just one or a few nearby input images.

PixelNeRF [35] (December 2020) introduces an additional image feature, which is extracted from pretrained neural networks, into a NeRF network. The image features are extracted from the feature volume by using projection and interpolation along a target camera ray with view direction. The features, view direction, and query points are then passed into the NeRF network to produce color and density. MVNeRF [68] (March 2021) builds a cost volume by warping 2D image features of the input images to a plane sweep volume on the reference view’s frustum for geometry-aware scene understanding, and combines this with physically based volume rendering for neural radiance field reconstruction. They jointly optimize the 3D feature volume and the NeRF MLP during training. Experiments show that MVNeRF trained in 15 minutes is comparable to baseline NeRF trained over hours on the DTU dataset. Follow-up works [124], [124], [131], [132] use a similar idea of using image features from pretrained networks as a prior conditioning for NeRF volume rendering.

Different from the aforementioned studies, RegNeRF [133] (December 2021) aims to solve the sparse-view problem by employing additional regularisations. The depth smoothness encourages piece-wise smoothing of geometry. The color regularization is achieved by estimating and maximizing the likelihood of rendered patches. SinNeRF [134] uses image warping and known camera parameters to create reference depth for depth supervision of unseen views. They use adversarial training to provide patch-wise texture supervision. Besides, there are also a few methods [135], [136] approach the sparse view goal by using point clouds for depth supervision.

All the aforementioned methods typically require explicit geometric inductive biases introduced by volume rendering. In contrast, the *geometry-free approaches* (e.g. LFN [99] and SRT [100]) have achieved results competitive with 3D-aware methods in the “few-shot” setting. The number of conditioning views is limited (*i.e.*, 1-10 images vs. dozens of images as in the usual NeRF setting).

#### 4.5 From Calibrated to Uncalibrated

For training NeRFs, most methods capture multiple images of a static scene in a controlled situation. The images are with corresponding known camera intrinsic and extrinsic parameters (posed) and are collected or captured under a constrained environment (constrained). However, real-life photographs of the same scene often do not have camera poses available and may contain per-image appearance variations due to lighting, weather, as well as transient or moving objects. We refer to these application scenarios as *uncalibrated*, where the images are unposed and contain per-image appearance variations.

**Unknown camera poses:** Many NeRF models [7], [68], [134] require known camera poses for training. In the original paper [7], unknown poses are acquired by the COLMAP library [74], which is also often used in many following

NeRF models without camera poses. Recent methods propose to build NeRF models without precomputed camera pose as given inputs for 3D novel view synthesis [37], [42], [71], [137], [138]. Instead, they jointly estimate camera poses alongside the training of the neural radiance field, which is formulated as an offline structure from motion (SfM) problem or an online simultaneous localization and mapping (SLAM) problem.

NeRF— [37] (February 2021) jointly optimizes the camera parameters and scene representation, eliminating the need of pre-computing camera parameters, while achieving view synthesis results on par with the COLMAP-enabled NeRF baseline. However, due to limitations with pose initialization, NeRF— is suited for front-facing scenes, but struggles with rotational motion and object tracking movements. Bundle-Adjusted Neural Radiance Field (BARF) [42] (April 2021) also builds NeRF and estimates camera poses simultaneously. BARF also uses a coarse-to-fine registration by adaptively masking the positional encoding. Jeong *et al.* [71] (August 2021) introduce a Self-Calibrating joint optimization NeRF (SCNeRF) model. Their camera calibration model can optimize not only unknown poses but also camera intrinsic for non-linear camera models such as fish-eye lens models. By using curriculum learning, they gradually introduce the nonlinear camera/noise parameters to the joint optimization. The camera optimization model is modular in design and could be applied to a variety of NeRF models. On the other hand, GNeRF [138] uses pose as the generative latent code. This method obtains coarse camera poses and radiance fields through adversarial training. This is done by using a generator which takes a randomly sampled pose, and synthesizes a view using NeRF-style rendering. A discriminator then compared the rendered view with the training image. An inversion network then takes the generated image and outputs a pose, which is compared to the sampled pose. This results in a coarse image-pose pairing. The images and poses are then jointly refined via a photometric loss in a hybrid optimization scheme.

**Per-image appearance variations:** NeRFs have been demonstrated to synthesize realistic novel images for small scenes in controlled settings. However, the appearance of real-world images may vary due to changes in lighting, weather [31], and transient objects [139]. NeRF models need to be improved in order to be able to train on these images, especially when NeRF is applied to large-scale scenes from a single object. This is especially important when applying NeRF from a single object to a large-scale scene, where the images can only be captured over months under different environmental conditions. For training with unconstrained photo collections, Martin-Brualla *et al.* propose NeRF in the Wild (NeRF-W) [31] (August 2020). In NeRF-W, the density MLP keeps fixed for all images in a scene while the color MLP is conditioned on a per-image appearance feature. Transient objects’ color and density functions are predicted by an additional MLP conditioned on per-image transient features. Generative Latent Optimization is used to construct these latent features. Based on the efforts of training NeRFs using unconstrained images, many methods extend the applicable scenarios from a small scene to a large-

scale urban or city scene.

#### 4.6 From Small to Large-scale

Recent methods have been demonstrated impressive view synthesis results for small scenes in controlled settings, including 360 degree capture of bounded scenes [7] and forward-facing capture of bounded and unbounded scenes [37]. Recent methods expand NeRF from a single object or a indoor bounded scene to an outdoor unbounded large-scale scene. These outdoor scenes also posed additional challenges in image-by-image variation in lighting and appearance.

NeRF++ [33] (October 2020) is developed for 360 degree captures within a large-scale unbounded 3D scene by separating this scene using a sphere. All foreground objects and fictitious camera views appear inside the sphere, whereas the background is outside. The outside of the sphere is reparametrized using an inverted sphere space. Two separate NeRF models are trained, one for the inside and one for the outside of the sphere. The camera ray integral is also evaluated in two parts.

A few methods [49], [55], [101], [140] apply NeRF-based 3D reconstruction and novel view synthesis to urban-level outdoor environments. Urban Radiance Field [49] (November 2021) makes three modifications to tailor NeRF model to the street view setting and to tackle the challenges. To compensate for the sparsity of viewpoints in such large-scale and complex scenes, they use sparse multi-view images supplemented by asynchronously captured LiDAR data as input. To address exposure variation between captured images, they estimate an affine color transformation for each camera as the automatic compensation for varying exposure. To provide a well-defined supervision signal for camera rays pointing at the sky area, they segment sky pixels and define a separate dome-like structure.

Mega-NeRF [141] (December 2021) performs urban-scale reconstruction and novel view synthesis from aerial drone images. It uses the inverse sphere parameterisation of NeRF++ [33] to separate background / foreground and incorporates the per-image appearance code of NeRF-W [31]. An ellipsoid is used to better fit the aerial point of view. An urban scene is divided into cells that each has a NeRF module. Each module is trained only on images with potentially relevant pixels. Colors and densities are first coarsely rendered and then refined dynamically through additional model sampling.

Block-NeRF [55] (February 2022) scales NeRF to render city-level scenes spanning multiple blocks by decomposing the scene into independently trained NeRFs. In this way, the rendering time can be decoupled from scene size, allowing the rendering of arbitrary large environments as well as per-block environment updates. To handle data collected over months under different environmental conditions, Block-NeRF is implemented with several modifications: 1) adding appearance code, pose refinement, controllable exposure to each separate NeRF, and 2) introducing a procedure of appearance alignment to allow the seamless combination of adjacent NeRFs. This design allows Block-NeRF to render entire neighborhoods of San Francisco.

S-NeRF [140] and BungeeNeRF (CityNeRF) [101] also address urban-level 3D reconstruction and novel view synthesis, albeit from remote sensing images. S-NeRF [140] (April 2021), denoting Shadow-aware NeRF, is proposed for multi-view satellite photogrammetry of earth observation scenes. It extends the NeRF approach to accommodate varying light conditions both from a directional light source (the Sun) and a diffuse light source (the sky). Direct illumination from the Sun is learnt as a local light source visibility field. Indirect illumination from a diffuse light source is represented as a non-local color field depending on the Sun’s position. To enable rendering across drastically-varied scales (from 6,300 km to 290 m), BungeeNeRF [101] (December 2021) proposes a progressive neural radiance field. In each training stage, the training set is gradually expanded by one closer scale, and the model is synchronously grown by multiple output heads for different levels of detail.

#### 4.7 From Static to Dynamic

The original NeRF assumes rigid objects, static scenes, and fixed illumination, which estimates only the resulting radiance along a ray after all light transport has occurred in a scene. A natural solution for dynamic scenes with moving objects and changing lights would be to create a separate NeRF-based model for each new scene configuration. In some cases, the subject may be *non-rigid* and *deformable*, such as a human body with movement [97], [142] or a face with expression [125]. Geometries vary when shapes and motion are non-rigid and deformable. We have discussed some methods aimed at handling varying lighting and moving objects in the previous sections. This section focuses on dynamic scenes with non-rigid and deformable objects [97], [98], [125], [142], [143], [144], [145], [146], [147], [148]. In literature, this line of research is often referred to as spatial-temporal view synthesis [145], [147].

For example, D-NeRF [97] (November 2020) extends NeRFs to a dynamic domain, which allows an image of an object to be modeled and rendered from a camera moving around a scene. They take time as an additional input, and split the learning process into two main stages: one encoding the scene into a canonical representation and another mapping it into the deformed scene at a particular time. The D-NeRF renders novel images, controlling both the camera view and the time variable. Neural Scene Flow Fields (NSFF) [145] (November 2020) models the dynamic scene as a time-variant continuous function of appearance, geometry, and motion. This representation is optimized through a neural network to fit the observed input views. Nerfies [98] (November 2020) extends NeRF by optimizing an additional continuous volumetric deformation field that warps each observed point into a canonical 5D NeRF. Inspired by principles of geometry processing and physical simulation to NeRF-like models, they propose an elastic regularization of the deformation field to improve robustness. Nerfies can turn casually-captured selfie photos or videos into a deformable NeRF, which allows for photorealistic renderings of the subject from arbitrary viewpoints. Xian *et al.* [144] (November 2020) learn a spatio-temporal neural irradiance field for dynamic scenes from a single video. This learned representation enables free-viewpoint rendering of the input video. They constrain the

TABLE 5

Comparison of 3D novel view synthesis methods using different 3D neural representations. The rows indicate whether each method 1) has been demonstrated to work with real world data, 2) is generalizable from a training set to novel scenes, 3) performs real-time inference, 4) works with very sparse (one or few) input images, 5) works without known camera poses at test time, 6) supports images with variations in appearance of the same scene, 7) handles dynamic scenes, or 8) accommodates large-scale scenes.

|                       | 3D-structured neural scene representation |               |             |           |                |           |              |                |              |                |                |                |          |             | Geometry-free |            |                 |          |         |          |           |   |
|-----------------------|---|---------------|-------------|-----------|----------------|-----------|--------------|----------------|--------------|----------------|----------------|----------------|----------|-------------|---------------|------------|-----------------|----------|---------|----------|-----------|---|
|                       | NeRF-based                                |               |             |           |                |           |              |                |              |                |                |                |          |             | Others        |            |                 |          |         |          |           |   |
|                       | NeRF [7]                                  | FastNeRF [40] | NeRF-W [31] | BARF [42] | DietNeRF [123] | GRF [127] | IBRNet [126] | PixelNeRF [35] | MVSNerf [68] | CodeNeRF [117] | NeRF-VAE [118] | BlockNeRF [55] | URF [49] | D-NeRF [97] | Nerfies [98]  | 3DiM [102] | DeepVoxels [16] | SRN [19] | DVR [9] | LFN [99] | SRT [100] |   |
| 1) Real-world data    | ✓   | ✓             | ✓           | ✓         | ✓              | ✓         | ✓            | ✓              | ✓            | ✓              | ✓              | ✓              | ✓        | ✓           | ✓             | ✓          | ✓               | ✓        | ✓       | ✓        | ✓         | ✓ |
| 2) Generalization     | ✓   | ✓             | ✓           | ✓         | ✓              | ✓         | ✓            | ✓              | ✓            | ✓              | ✓              | ✓              | ✓        | ✓           | ✓             | ✓          | ✓               | ✓        | ✓       | ✓        | ✓         | ✓ |
| 3) Real-time          | ✓   | ✓             | ✓           | ✓         | ✓              | ✓         | ✓            | ✓              | ✓            | ✓              | ✓              | ✓              | ✓        | ✓           | ✓             | ✓          | ✓               | ✓        | ✓       | ✓        | ✓         | ✓ |
| 4) Few images         | ✓   | ✓             | ✓           | ✓         | ✓              | ✓         | ✓            | ✓              | ✓            | ✓              | ✓              | ✓              | ✓        | ✓           | ✓             | ✓          | ✓               | ✓        | ✓       | ✓        | ✓         | ✓ |
| 5) Pose-free          | ✓   | ✓             | ✓           | ✓         | ✓              | ✓         | ✓            | ✓              | ✓            | ✓              | ✓              | ✓              | ✓        | ✓           | ✓             | ✓          | ✓               | ✓        | ✓       | ✓        | ✓         | ✓ |
| 6) Varying appearance | ✓   | ✓             | ✓           | ✓         | ✓              | ✓         | ✓            | ✓              | ✓            | ✓              | ✓              | ✓              | ✓        | ✓           | ✓             | ✓          | ✓               | ✓        | ✓       | ✓        | ✓         | ✓ |
| 7) Large-scale        | ✓   | ✓             | ✓           | ✓         | ✓              | ✓         | ✓            | ✓              | ✓            | ✓              | ✓              | ✓              | ✓        | ✓           | ✓             | ✓          | ✓               | ✓        | ✓       | ✓        | ✓         | ✓ |
| 8) Dynamic            | ✓   | ✓             | ✓           | ✓         | ✓              | ✓         | ✓            | ✓              | ✓            | ✓              | ✓              | ✓              | ✓        | ✓           | ✓             | ✓          | ✓               | ✓        | ✓       | ✓        | ✓         | ✓ |

time-varying geometry of the dynamic scene representation using the scene depth estimated from video depth estimation methods, aggregating contents from individual frames into a single global representation. Neural Radiance Flow (NeRFlow) [147] (December 2020) is to learn a 4D spatial-temporal representation of a dynamic scene from a set of RGB images. The key idea is the use of a neural implicit representation that learns to capture the 3D occupancy, radiance, and dynamics of the scene. NeRFlow enables multi-view rendering in diverse dynamic scenes, including real images, water pouring, and robotic interaction. Non-Rigid Neural Radiance Fields (NR-NeRF) [146] (December 2020) is a reconstruction and novel view synthesis approach for general non-rigid dynamic scenes. It takes images of a dynamic scene (*e.g.*, from a monocular video) as input, and creates a high-quality space-time geometry and appearance representation. HyperNeRF [143] (June 2021) extends the canonical space in Nerfies [98] to a higher dimension, and adds an additional slicing MLP to describe the 3D representation using ambient space coordinates. The canonical coordinate and ambient space coordinate are then used to condition baseline NeRF models’ density and color MLPs. HyperNeRF achieves excellent results in synthesizing views when scenes contain topological changes, such as a person opening the mouth and a banana being peeled. CoNeRF [148] (December 2021), built on HyperNeRF, allows sliders to easily edit face images. Slider values are provided to an MLP-parameterized per-attribute Hypermap deformation field. It achieves remarkable results, showing broad commercial applications for virtual human avatars. The Fourier Plenocree [142] (February 2022) proposes to use frequency domain to encode time-dependent information for dynamic scenes. It first constructs a coarse visual hull built from sparse views predicted by a generalization of NeRF and Shape-From-Silhouette. Colors and densities are then densely sampled inside this hull and stored in a coarse Plenocree. Views are sampled from the Plenocree and transmissivity thresholding is used to remove empty points. The Plenocree is updated with new leaf densities and spherical harmonics (SH) color coefficients for the remaining points. A Fourier transform MLP is then used to extract Fourier coefficients of the density and SH color coefficients. These coefficients are passed into an inverse discrete Fourier

transform to restore SH coefficients and density. Gafni *et al.* [125] (December 2022) learn a dynamic neural radiance field to model a 4D facial avatar from a monocular video of a person. It allows for novel head pose synthesis and facial expression editing.

## 5 3D-AWARE GENERATIVE MODELS

In recent years, neural scene representations have lifted image generation into 3D settings with explicit camera control. Early methods based on voxel representations [15], [17], [18], [22], [149] typically fail to synthesize the complex scenes and photo-realistic details due to the limited grid resolutions. Their learnable rendering modules produce view-inconsistent and degraded results, and cannot be generalized to unseen camera positions. In contrast, implicit neural representations, especially NeRFs, have proven to generate high-fidelity novel-view results from a multiple-view image collection. These methods are usually proposed for 3D novel view synthesis [7], [39], [73], which follows a per-scene training on multi-view image collections of one scene. We have introduced this category of studies in Sec. 4.

Inspired by these 3D novel view synthesis methods, follow-up works introduce the efficient and expressive implicit neural representations to the field of 2D generative image synthesis, leading to a new paradigm called 3D-aware generative models [2], [30]. These methods do not assume a large number of posed images of a single scene. Instead, they learn a model for synthesizing novel scenes by training on unposed and unstructured image collections. These 3D-aware generative models, mostly 3D GANs, follow a same experimental setting as their 2D counterparts, *i.e.*, generating high quality photo-realistic results from single-view image datasets, with an extra goal to ensure 3D consistency across multiple views. 3D GANs, an outstanding representative of 3D-aware generative models, utilize an adversarial framework to train a generative model for these representations, which synthesize novel scenes by training on unlabeled and unposed single-view images without 3D supervision. However, despite 3D-consistent results, their computational constraints limit the rendering resolutions and quality, making it difficult to train on high-resolution images. For high-quality high-resolution image

synthesis, recent methods turn to find more efficient and more expressive representation or improve the rendering efficiency and consistency.

In this section, we first introduce the unconditional 3D-aware generative networks based on different neural scene representations in Sec. 5.1. We especially emphasize their efforts towards: 1) learning efficient and expressive geometry and appearance representations (Sec. 5.1.1); 2) developing accelerated and view-consistent rendering algorithms (Sec. 5.1.2); and 3) real-time and user-interactive editing (Sec. 5.1.3). We then present conditional 3D-aware generative models [59], [63], [69], [150], [151], [152] in Sec. 5.2.

In 2D GANs, “unconditional” methods are referred to as those merely inputting latent codes that are sampled from a prior distribution. In this survey, we use “unconditional” 3D-aware generative models to refer to those using latent codes and camera positions as input. In some cases, the camera positions could also be generated from the randomly-sampled latent codes instead of human-understandable control factors. Those taking other inputs, especially image, semantic label or sketch, are the conditional ones.

Here is a clarification of the defined terminology and the differences between the two kinds of methods in Sec. 4 and in this section. Both aim to generate multi-view-consistent and photo-realistic images, using a similar pipeline that first learns the 3D representation and then renders it from that viewpoint (see Fig. 5). It is their application scenarios and training data that differentiate the two kinds of methods. As with their 2D counterparts, 3D-aware generative models generate images from a collection of single views, while 3D novel view synthesis learns a 3D representation from multiple views of a scene. The term *3D-aware generative models* may also be used to refer to 3D novel view synthesis methods, but this survey uses this term only in reference to the methods trained on single view images.

The majority of methods in this part belong to the category of generative adversarial networks. Other kinds of generative models, especially diffusion models [153], [154], [155], [156], [157], [158], which have proven extremely effective in generating high-quality images in recent years, have not yet been widely applied to 3D-aware image synthesis. Only a few very recent studies are based on diffusion models [102] for 3D novel view synthesis. Some use generative latent optimization [48], [159] instead of adversarial training [160]. These generative models are expected to catch up in the near future.

## 5.1 Unconditional 3D Generative Models

Like 2D GANs, 3D-aware GANs have recently achieved tremendous breakthroughs in terms of image quality and editability for 2D image synthesis, with the extra goal of 3D consistency by introducing explicit camera control. These methods can be formulated in the form of  $I = f(z, \theta)$ , where the noise vector  $z$  is for appearance and  $\theta$  means camera pose. Towards editable, high-resolution, and view-consistent image synthesis, proposed methods mainly work on two key components: 1) to learn efficient and expressive representations of geometry and appearance; 2) to develop accelerated and view-consistent rendering algorithms.

### 5.1.1 Learning Efficient and Expressive Geometry and Appearance Representations

Early 3D GANs adopt voxel-based representation [15], [17], [18], [22], [149]. For example, VON [17] (December 2018) and PrGANs [15] (December 2016) first learn an explicit shape and render images at different viewpoints. They are trained under 3D supervision (as such they are also categorized into using 3D priors as constraints, which is introduced in Sec. 3.3). PlatonicGAN [149] (November 2018) learns a generative 3D model from an unstructured collection of 2D images. The learned shape and its rendered images are limited to low resolutions and coarse detail due to the computational complexity. The approaches using deep-voxel representations [18], [22] can create finely-detailed images under different poses. HoloGAN [18] (April 2019) first uses 3D convolutions to learn a deep-voxel representation (in a canonical pose), then utilizes a rigid-body transformation (3D rotation) to transform this representation to a certain pose, and finally applies a projection unit to render an image. In contrast to HoloGAN, which learns 3D features directly for the entire scene, BlockGAN [22] learns 3D features for each object separately. BlockGAN (February 2020) decomposes a 3D scene into two components: the background and one or more foreground objects. It uses multiple noise vectors  $z_i$  for the background and each foreground object. This design disentangles a scene into separate objects and enables control over camera pose, lighting, and shadow. However, the early voxel-based methods [15], [17], [18], [22], [149] fail to synthesize the complex scenes and photo-realistic details due to the limited grid resolutions. Their reliance on a learned black-box rendering leads to discretization artifacts, degrades view-consistency of the generated images, and makes generalization to unseen camera poses difficult. Liao *et al.* [44] (December 2019) use 3D primitives as abstract object representations and differentiable rendering to project the 3D representations onto the image plane where a 2D generator transforms them into object appearances and composites them into a coherent image.

These previous methods typically fail to synthesize the complex scenes and photo-realistic details due to the limited expressiveness and efficiency. Implicit neural representations (INR), especially NeRFs, which have proven to generate high-fidelity results in novel view synthesis, are also introduced to 3D-aware generative models [2], [30]. These vanilla implicit scene representations typically assume a large number of *posed* images of a single scene for training. To avoid the requirement of posed images, an increasing number of methods [1], [2], [30], [34], [50], [52] turn to utilize an adversarial framework to train a generative model for these representations from *unposed* images. The visualization results from COLMAP [74] (a multi-view stereo algorithm) validate those methods showing greater 3D consistency than the voxel-based representations.

GRAF [30] (July 2020) proposes to use NeRF [7] to represent the scene. To loose the constraint of a large number of posed images of a single scene for training, it uses an adversarial framework to train a generative model for radiance fields from unstructured images. The generator  $G_\theta$  takes camera matrix  $\mathbf{K}$ , camera pose  $\xi$ , 2D sampling

pattern  $\nu$  and shape/appearance codes  $\mathbf{z}_s \in \mathbb{R}^m / \mathbf{z}_a \in \mathbb{R}^n$  as input and predicts an image patch  $\mathbf{P}'$ . The discriminator  $D_\phi$  compares the synthesized patch  $\mathbf{P}'$  to a real patch  $\mathbf{P}$  extracted from a real image  $\mathbf{I}$ . One significant modification is that GRAF makes NeRF conditioned on two additional latent codes: a shape noise  $z_s$  and an appearance noise  $z_a$ . The conditional radiance field is implemented as a multi-layer perceptron (MLP) with a pre-defined positional encoding and is the only component with trainable parameters. For computational and memory efficiency, GRAF further introduces ray sampling and 3D point sampling, leading to a sparse 2D sampling patterns of size  $K \times K$  pixels. A follow-up work pi-GAN [2] (December 2020) differs from GRAF in three ways on network architecture and training strategy: 1) pi-GAN use SIREN [161] as a choice of neural implicit representation rather than a positionally-encoded ReLU MLP [7]; 2) pi-GAN leverages a StyleGAN-inspired mapping network to condition layers in the SIREN on a single input noise code through feature-wise linear modulation (FiLM) instead of conditioning on two additional shape/appearance codes; 3) pi-GAN follows ProgressiveGAN [85] where discriminator grows progressively rather than a patch-based discriminator. Built similarly to pi-GAN [2], LOLNeRF [48] (November 2021), which is capable of single-shot view synthesis of human faces, uses generative latent optimization [159] instead of adversarial training [160]. GIRAFFE [34] improves the BlockGAN [22] framework by replacing the voxel-based representation and 3D-to-2D projection with a NeRF-based compositional 3D scene representation and a neural rendering pipeline. It can rotate, translate, scale each object and change camera poses but with compromised image quality and resolution. Compared to 2D generative models, these models take much more calculations to render an image (speed) and require much more memory during training to cache intermediate results (memory). The computational constraints that have limited the rendering resolutions and quality.

For high-quality image synthesis (towards  $512 \times 512$  and beyond), recent methods turn to find more efficient and expressive representation, improve the training efficiency, or the combination of both. We focus on learning efficient and expressive representations as follow in this subsection, leaving the discussion of the later parts to the next subsection.

CIPS-3D [46] (October 2021) adopts a shallow NeRF network (containing only three SIREN blocks [161]) to represent 3D shape and a deep 2D INR network to synthesis high-fidelity appearance. Inspired by recent progress in 3D surface reconstruction, GOF [47] (November 2021) combines implicit surfaces and radiance fields. They reinterpret the alpha values in the rendering equation as occupancy representations and reformulate generative radiance fields by predicting alpha values instead of volume densities. EG3D [50] (December 2021) proposes a tri-plane hybrid 3D representation, formulated from the explicit features of the StyleGAN2 generator. They align explicit features along three axis-aligned orthogonal feature planes and query any 3D position by projecting it onto each of the three feature planes, resulting in an aggregated 3D feature. The aggregated 3D features are then interpreted as color and

density by an additional lightweight decoding network. The proposed tri-plane representation is 3 to 8 times faster than an implicit Mip-NeRF [39] network and only requires a fraction of its memory. A super-resolution module upsamples and refines raw neurally rendered images. This tri-plane representation has been used in many follow-up studies [62], [63].

VolumeGAN [53] (December 2021) explicitly learns a structural representation and a textural representation. It learns a feature volume to represent the underlying structure, which is transformed into a feature field based on a NeRF-style model. The feature field is then aggregated into a 2D feature map as the textural representation. A neural renderer is finally used for appearance synthesis. StyleSDF [52] (December 2021) merges a SDF-based 3D representation into the 2D StyleGAN generator. This framework consists of two main components: a backbone conditional SDF volume renderer and a StyleGAN generator. The renderer takes in a latent code and camera parameters, queries points and view directions within the volume, and projects 3D surface features onto 2D views. StyleGAN generates high-resolution images based on the projected features. SDF serves as a proxy for the density function used in the traditional volume rendering. The incorporation of SDFs provides clear surface definition, allowing marching cubes [10] to extract the mesh. More importantly, the use of SDFs along with the related losses leads to higher quality geometry in terms of view-consistency and expressiveness, even with a simplified volume sampling strategy. To overcome the drawbacks of GIRAFFE [34] and inherit its 3D controllability, a follow-up work GIRAFFE-HD [162] (March 2022) leverages a style-based neural renderer, generates the foreground and background independently, and stitches them together to composite a coherent final image. It enforces semantic disentanglement and 3D consistency through training constraints.

In contrast to previous methods, VoxGRAF [61] (June 2022) adopts a 3D-aware GAN based on a sparse scene representation that allows for efficient rendering. It parameterizes the radiance field on a sparse voxel grid rather than using a coordinate-based MLP and predicts colors and density values on this sparse voxel grid using volume rendering. GMPI [64] (July 2022) makes a classical 2D GAN, *i.e.* StyleGAN2, 3D-aware by only introducing 1) a multiplane image style generator branch which produces a set of alpha maps conditioned on their depth; and 2) a pose conditioned discriminator.

### 5.1.2 Improving Rendering Efficiency and Consistency

Early studies [18], [22] use simple 3D-to-2D projections for rendering. Such operations fail to produce high-quality images with fine-grained details and are restricted to representing poses in the training dataset. For higher rendering quality, recent methods adopt the state-of-the-art neural volume rendering techniques. GRAF [30] and pi-GAN [2] implements a discretized form of the volume rendering equation and uses the stratified and hierarchical sampling approach introduced by NeRF. The neural volume rendering approach has several advantages over previous 3D-to-2D projections: 1) producing images with fine details and high resolutions and 2) allowing for explicit control over camera pose, focal length, aspect ratio, and other

parameters. Despite the advantages, the volume integrations approximated by sampling points along viewing rays are still costly for both training and inference. Training a 3D GAN requires rendering tens of millions of images. Using these representations for neural volume rendering is not suitable for training high-resolution GANs due to the expensive sampling and MLP queries.

Some studies work on improving the rendering speed and consistency. To reduce the high memory and computation cost, along with learning more efficient representations as introduced in the previous section, recently developed 3D-aware GANs make use of a two-stage rendering process [1], [34], [50], [52], [53], [162] or develop efficient volume rendering strategy [45], [46], [51]. Meanwhile, aimed to reduce view-inconsistent artifacts brought by the 2D renderers, they adopt different strategies such as NeRF path regularisation [1] and dual discriminators [50]. We introduce these methods as follows.

**Two-stage Rendering Process:** Some methods render the 3D representation directly at the final image resolution [2], [61]. Due to the high memory and computation cost of volume rendering, direct rendering at target resolution is not efficient and struggles to generate images at high-resolution results (512×512 and beyond). Therefore, an alternative solution is to use a two-stage rendering process [1], [34], [50], [52], [53], [162]. They render a low-resolution feature map with ray marching and use a neural renderer to decode it into a high-resolution image. Typically, they first generate a feature map at a low resolution and then employ upsampling in 2D space to progressively increase into the required high resolution. Niemeyer *et al.* [34] improve training and rendering efficiency by combining NeRF with a ConvNet-based renderer. Similarly, Chan *et al.* [50] perform the majority of the training at a rendering resolution of 64×64 and gradually increase the resolution, pixel-by-pixel, to 128×128, which are fed into a super-resolution module to produce images at the target resolution. However, these pixel-wise learnable upsamplers sacrifice view consistency and impair the quality of the learned 3D geometry due to the particular network designs. In contrast, non-learnable upsamplers that interpolate the feature map with predefined lowpass filters (*e.g.* bilinear interpolation) produce smoother results but lead to non-removable bubble artifacts. In StyleNeRF [1], the two approaches are combined to balance quality and consistency.

Despite that upsampler scales the intermediate result to high resolution, it comes with two severe limitations: 1) the texture and shape change as the camera moves; 2) the geometry is represented in a low resolution ( $\approx 64^3$ ), both resulting in a compromised multi-view consistency of a generated object. To overcome the above limitations of the two-stage rendering, Skorokhodov *et al.* [62] drop the upsampler and improve the patch-wise optimization strategy [30] to build a 3D generator. Patch-based discriminator is introduced for 3D GAN training in GRAF [30], where the generated patch is compared with a real image patch. Based on the same patch-wise fashion, they redesign the discriminator by making it better suited to operating on image patches of variable scales and locations, along with changing the random scale sampling strategy from

an annealed uniform to an annealed beta distribution. This allows their proposed EpiGRAF to converge 2-3 times faster than the upsampler-based architectures despite the generator modeling geometry in full resolution.

**Efficient Rendering Strategy:** This part can be categorized into two groups of approaches according to their adopted strategies. The first group is to use lightweight decoder [50] or a simplified sampling strategy [52] thanks to the usage of an efficient and expressive representation. In StyleSDF [52], their usage of SDFs as 3D representations leads to higher expressiveness and view-consistency, allowing a simplified volume sampling strategy for rendering. Unlike using stratified sampling in previous methods [1], [2], [7], [30], they split integration intervals  $[t_n, t_f]$  into  $N$  evenly-sized bins, draw a single offset term uniformly  $\delta \sim \mathcal{U}[0, \frac{t_f-t_n}{N}]$ , and sample  $N$  evenly-spaced points,  $t_i = \frac{t_f-t_n}{N} \cdot i + \delta$ , where  $i \in \{0, \dots, N-1\}$ . Their totally discarding hierarchical sampling reduces the number of samples by 50%. VoxGARF [61] accelerates the rendering from the perspective of spatial sparsity, where volume rendering yields a foreground image and an alpha mask.

The second group aim to develop efficient sampling strategy [45], [47], [51]. They aim to constrain the point sampling in a reduced space rather than anywhere in the volume. GRAM [51] proposes a manifold predictor  $\mathcal{M}$  to predict a reduced space for point sampling and radiance field learning.  $\mathcal{M}$  is a light-weight MLP that maps a point  $\mathbf{x}$  to a scalar value  $s$ . The predicted scalar field gives  $N$  isosurfaces with a set of predefined levels (constant values  $\{l_i\}$ ):  $\mathcal{S}_i = \{\mathbf{x} \mid \mathcal{M}(\mathbf{x}) = l_i\}$ . The rendering only samples points from intersections between the determined isosurfaces and a camera ray. Several methods are developed to achieve more efficient volume rendering based on the observation that the renderer can just sample points near the surface to save computation if the rough surface position is known beforehand. Pan *et al.* [45] introduce a light-weighted surface tracking network  $\mathcal{S}$  to estimate the rendered object surface. It narrows the interval for volume rendering and reduces the number of points used for rendering accordingly. This saves rendering computations by just querying points near the predicted surface. Instead of predicting volume densities in the cumulative rendering process, Xu *et al.* [47] reformulate generative radiance fields by predicting the alpha values directly. The intermediate alpha values used for numerical stability in the rendering equation inherently fall in a fixed value range  $[0, 1]$  and can be therefore interpreted as occupancy values. This allows gradually shrinking the sampling region of each camera ray. The sample region in the cumulative rendering process shrinks from the entire volume to a narrow interval around the surface.

**Consistent View Regularisation:** The view-inconsistencies could be caused by colors and shapes. Some methods propose multi-view regularisations on colors and shapes to improve photometric and geometric consistencies. In other sense, this goal is also equivalent to improving the surface and texture quality. Many methods adopt different strategies to reduce view-inconsistent artifacts brought by the 2D renderers, including path regularisation [1], dual discriminators [50], or rendering under different

lighting conditions [45]. For example, Gu *et al.* [1] propose a NeRF path regularisation to enforce 3D consistency, which is implemented by sub-sampling high-resolution output of StyleNeRF and comparing them against the low-resolution image generated by NeRF. Chan *et al.* [50] propose a pose-conditioned dual discriminators [50], [61] with two modifications traditionally seen in GAN discriminators. First, they pass the rendering camera intrinsics and extrinsics matrices to the discriminator as a conditioning label. Second, they take as the input the concatenation of the final result  $I_r$  and a low-resolution RGB image  $I'_r$ . They interpret the first three feature channels of a neurally rendered feature image as  $I'_r$  and bilinearly upsample it to the same size of  $I_r$ . This pose-conditioned dual discriminator is used in many follow-up studies. Shi *et al.* [163] design a geometry-aware discriminator, GeoD, to improve 3D-aware GANs. Besides the real/fake classification, they assign the discriminator an additional geometry branch, aiming to derive the shape-related information (e.g. depth and normal), which is employed as an extra signal to supervise the generator.

In [45], Pan *et al.* observe that small variations of shape could lead to similar RGB images that look equally plausible to the discriminator, as the color of many objects is locally smooth. Optimizing the radiance fields from a set of 2D training images can encounter critical degenerate solutions in the absence of geometry constraints, leading to a multi-view inconsistency problem in NeRF-based generative models. This phenomenon is referred to as shape-radiance (color) ambiguity. To eliminate this problem, they propose to render under different lighting conditions [45]. This multi-lighting constraint is realized by modeling illumination explicitly and performing shading with various lighting conditions. To overcome the same issue, MVCGAN [58] (April 2022) builds geometry constraints by optimizing multiple views jointly to ensure geometry consistency between views. They minimize re-projection loss between a primary image and a warped image, and integrate a stereo mixup module to encourage the warped image to be similar to a real image. Such scheme guarantees geometry constraints between different views and supports large pose variations.

### 5.1.3 Facilitating User-interactive Editing

Plenty of approaches are proposed to facilitate user-interactive editing. They can change the background’s appearance independent of the foreground, translate or rotate the foreground object in 3D, and change the foreground object’s shape and color. For example, some methods [22], [34], [162] use multiple noise vectors  $z_i$  to represent the background and each foreground object. Unlike previous studies that learn 3D features directly for the whole scene [18], they learn a 3D feature for each object, render separately, and stitch them together to composite a coherent final image. Such design disentangles a scene into separate objects and enables control over camera pose, lighting, and shadow.

Differently, Kwak *et al.* [65] design a layer-wise Subspace in INR NeRF-based generator (SURF-GAN). Instead of being used represent the background and each foreground object, multiple noise vectors are injected layer-by-layer into

NeRF-based SURF blocks, in which interpretable dimensions are captured in layers with sub-modulation vectors. SURF-GAN [65] includes several SURF blocks that take position and view direction as inputs to predict view dependent color. The SURF block in the  $i$ -th layer is formulated as  $\psi_{i+1} = \text{SURF}(\psi_i, \phi_i)$ , where  $\psi_i$  and  $\phi_i$  denote the input feature and modulation of  $i$ -th layer respectively. The modulation of each layer is decided by weighted summation of  $K$  sub-modulations with  $z_i: \phi_i = U_i D_i z_i + u_i$ . It consists of learnable matrices, orthonormal basis  $U_i = [u_{i1}, \dots, u_{iK}]$  and a diagonal matrix  $D_i = \text{diag}(d_{i1}, \dots, d_{iK})$ . Each column of  $U_i$  plays a role of sub-modulation and it is updated to discover a meaningful direction that results in semantic change in image space. Each  $d_i$  serves as a scaling factor of corresponding basis vector. With the  $k$  latent codes serving as  $k$  control parameters, SURF-GAN can control the discovered semantic attributes by manipulating corresponding elements.

IDE-3D [63] enables local control of the facial shape and texture and supports real-time, interactive editing. It makes two key modifications based on [50] to enable such interactive disentangled editing. First, they takes two (instead of one) codes respectively representing shape and texture, which are injected separately into the feature extraction network that gives spatially aligned 3D volumes of semantic and texture in the tri-plane representation. Second, given the generated 3D volumes, they jointly render rgb images (first three channels of the volume rendering outputs) and semantic masks (instead of just rgb images) through the volume rendering and a 2D CNN-based up-sampler. The dual discriminator is also changed accordingly to take as input the concatenation of resized low-resolution rgb/semantics image and the synthesised high-resolution rgb/semantics image.

In order to eliminate pose effect for portrait images, many methods [63], [65] also learn to map any given input the portrait images to a canonical view, either pre-trained [65] or jointly-trained [63]. A few methods also learn a canonical 3D representation [18], [50].

## 5.2 Conditional 3D Generative Models

The unconditional 3D GANs introduced in Sec. 5.1 typically lack the capability of performing precise attribute editing for real images. Similar to 2D generative models, 3D-aware image synthesis methods for real image editing could either use the aforementioned pretrained 3D-GANs via GAN inversion techniques or train the 3D GAN model from scratch with additional inputs.

As an emerging technique to bridge the real and fake image domains, GAN inversion [105] plays an essential role in enabling pretrained GAN models for applications of real image editing. GAN inversion inverts a real image into the latent space of a trained GAN model, which allows us to manipulate the image by varying the inverted code in the latent space for a certain attribute (known as the latent space traversals). Most GAN inversion are based the 2D pretrained GAN models due to their popularity in image synthesis during the past few years. However, with the emerging of 3D GAN technology, GAN inversion are also been applied to these model for real image editing [2],

[45], [63], [150], [152]. Some directly applies the existing GAN inversion and latent space traversal techniques for this goal, while others develop specially new tools for the 3D GANs. For example, FENeRF [150] (November 2021) has attempted to edit the local shape and texture in a facial volume by using an optimization-based GAN inversion [105]. ShadeGAN [45] (October 2021) could also be used to reconstruct a given image by performing GAN inversion. Such inversion with this method allows to obtain object properties from the image, such as shape, normal, albedo, and shading. Lin *et al.* [152] (March 2022) propose a method for multi-view consistent video editing and animation based on 3D GAN inversion. They invert the video frames into the latent space of a 3D GAN [2] by using pivotal tuning inversion (PTI) [164] and edit face attributes by using Style-Flow [107]. Nonetheless, the aforementioned methods either suffer from the low-resolution results or the time-consuming optimization-based inversion process. In IDE-3D [63], they adopt a hybrid GAN inversion approach. Given a facial image and its semantic label, IDE-3D obtains the texture and semantic latent codes with corresponding encoders and uses them as the initialization for the optimization-based PTI [164] to obtain high-fidelity reconstruction. Editing can be performed by directly drawing on the inverted semantic masks, given the optimized latent codes.

Other methods target at pose-dependent views by training a 3D network conditioned on a single image. Pix2NeRF [69] (February 2022) demonstrates that merely applying a learning-based GAN inversion technique (learning an encoder and keeping the generator fixed during training) is insufficient to obtain an accurate mapping from image to latent space with pi-GAN [2] as the backbone. Instead, they train the encoder jointly with a generator and a discriminator (both of the same architecture and procedure as in [2]). Once trained, given an input image, Pix2NeRF disentangles its pose and content and renders novel views of the content. Sem2NeRF [59] (March 2022) takes as input a single-view 2D semantic mask and outputs a NeRF-based 3D representation that can be used to render photo-realistic images in a 3D-aware view-consistent manner. AutoRF [151] (April 2022) focuses on novel view synthesis of objects without background. This model consists of an encoder that extracts a shape and an appearance code from an object’s image, which can be decoded into an implicit radiance field operating in normalized object space and leveraged for novel view synthesis. Object images are generated from real-world imagery by leveraging machine-generated 3D object detections and panoptic segmentation.

## 6 DISCUSSION

Despite great advances in 3D-aware image synthesis, many challenges remain and its rapid growth is expected to continue. In the following, we provide an overview of the future directions, problems to solve, and trends to anticipate. Due to their unique characteristics, some limitations or future trends may only apply to certain categories of methods.

**Quality:** Recent methods have proposed numerous strategies to ensure 3D consistency across multiple views, but results still seem unsatisfactory. Unlike the traditional

graphic rendering process, since implicit neural representations do not provide an explicit and holistic 3D shape for rendering, it seems inevitable that there will be inconsistencies in the generated surface and texture under different viewpoints. Moreover, these strategies are introduced separately rather than endogenously as part of the method. We expect that in the future there will be more endogenous approaches to 3D-aware image synthesis that generates high-quality, high-resolution, multi-view-consistent images in real time, as well as high-quality 3D geometry.

**Speed:** There is typically a slow training and inference speed with methods in Sec. 4 and Sec. 5. Most methods that attempt to accelerate training and inference time require extra memory for caching trained models or use additional voxel/spatial-tree based scene features. It is expected that future speed-based methods should develop memory-friendly frameworks as well as novel inclusive and learnable scene representations to accelerate training and inference.

**Editability:** In spite of the promising quality of the produced results, most methods are incapable of editing individual image components. In some methods, latent vectors are used at various points along the pipeline to control composition, shape, and appearance of images. The latent codes enable the model to control small changes in scene content, such as lighting or coloration, per image. Others allow additional input to change aspects of the scene, such as images, texts, semantic labels, or direct control parameters. The editability of 3D-aware image synthesis methods, however, still has plenty of room for improvement compared to their 2D counterparts.

**Forensics:** The success of recent generative models has led to many new applications, but also raised ethical and social concerns, such as fraud and fabricated images, videos, and news (known as deepfakes). The ability to detect deepfakes is essential to preventing malicious usage of these models. Recent studies have shown that a classifier can be trained to distinguish deepfakes and generalize to unseen architectures. It may continue to be a cat-and-mouse game in the future, since generated images will become increasingly difficult to detect. Conversely, these images can also be utilized as the training data for identifying fakes.

**Network Design:** Most current methods rely on a 2D architecture design that introduces 3D representation, rendering, and multi-view regularization to make a 2D model 3D-aware. The majority of 3D-aware generative models use convolution-powered generative adversarial networks. In recent years, transformer-based 2D image synthesis methods (*e.g.* StyleSwin [165]) have emerged corresponding to their counterparts in convolutional networks (*e.g.* StyleGANs [79], [81], [103], [104]). Developing 3D-aware generative models that are built on transformers with lighter structures and lower computational demands remains to be explored. Since almost all the methods above are based on GANs, developing other generative models that are 3D-aware, especially diffusion models, is also a promising future direction of research.

**Applicable Scenarios:** Like their 2D counterparts, current 3D-aware image synthesis methods exhibit state-of-the-art performance within narrow image domains. In most

cases, they either require per-scene training (see Sec. 4) or are restricted to images of certain types and structures, such as faces and bedrooms (see Sec. 5). Recent efforts have been made to generalize 2D GANs to complex scenarios. StyleGAN-XL [166], for example, scales StyleGAN to large datasets with multiple classes of objects. Self-Distilled StyleGAN [167] aims to use internet photo collections for training. These efforts can enable 3D-aware image synthesis for real-world scenarios, but the attendant computational complexity will need to be addressed.

**Evaluation metrics:** It remains to be explored whether there are any reliable metrics that can better evaluate the photorealistic and geometric quality of generated images. For the single-view evaluation, the general metrics for generative models are mainly used to measure image quality and diversity. The 3D consistency is determined by measuring the distances between (pseudo-)depth maps and the similarity between identities at different camera positions. However, considering the lack of real images as the reference, these calculated values on the generated results only partially reflect the stability of the generated results, but cannot reflect the distance from the real samples. In the multi-view evaluation, PSNR and SSIM are used for assessment when ground-truth rendering results are available. But the images used by recent methods are usually acquired under an unconstrained condition with varying illuminations and moving objects, meaning PSNR and SSIM being unavailable for calculation. There is still a lack of effective assessment tools to evaluate the difference between the predicted and expected outcomes in a more reliable and direct manner for 3D-aware image synthesis.

## 7 CONCLUSION

This paper presents a comprehensive overview of recent advances in generative 3D image synthesis. We propose a systematic taxonomy for 3D-aware image synthesis. Specifically, we categorize the existing approaches into three groups: 3D control of 2D generative models, 3D-aware generative models from single view image collections, and novel view rendering from multiple view image collections. We also identify some open problems on this topic, which we hope will inspire future research. We hope that this timely and up-to-date survey will serve as a starting point for future research to help advance this emerging and challenging field.

## REFERENCES

- [1] J. Gu, L. Liu, P. Wang, and C. Theobalt, "StyleNeRF: A style-based 3D aware generator for high-resolution image synthesis," in *ICLR*, 2022. [1](#), [4](#), [6](#), [7](#), [17](#), [19](#), [20](#)
- [2] E. R. Chan, M. Monteiro, P. Kellnhofer, J. Wu, and G. Wetzstein, "pi-GAN: Periodic implicit generative adversarial networks for 3D-aware image synthesis," in *CVPR*, 2021. [1](#), [4](#), [6](#), [7](#), [16](#), [17](#), [18](#), [19](#), [20](#), [21](#)
- [3] X. Pan, B. Dai, Z. Liu, C. C. Loy, and P. Luo, "Do 2D GANs know 3D shape? unsupervised 3D shape reconstruction from 2D image GANs," in *ICLR*, 2021. [2](#)
- [4] X. Pan, A. Tewari, L. Liu, and C. Theobalt, "GAN2X: Non-lambertian inverse rendering of image GANs," in *3DV*, 2022. [2](#)
- [5] L. Mescheder, M. Oechsle, M. Niemeyer, S. Nowozin, and A. Geiger, "Occupancy networks: Learning 3d reconstruction in function space," in *Proceedings of the IEEE/CVF conference on computer vision and pattern recognition*, 2019, pp. 4460–4470. [3](#), [12](#)
- [6] J. J. Park, P. Florence, J. Straub, R. Newcombe, and S. Lovegrove, "DeepSDF: Learning continuous signed distance functions for shape representation," in *CVPR*, 2019, pp. 165–174. [3](#), [12](#)
- [7] B. Mildenhall, P. P. Srinivasan, M. Tancik, J. T. Barron, R. Ramamoorthi, and R. Ng, "Nerf: Representing scenes as neural radiance fields for view synthesis," in *ECCV*, 2020. [3](#), [4](#), [5](#), [7](#), [12](#), [13](#), [14](#), [15](#), [16](#), [17](#), [18](#), [19](#)
- [8] S. Peng, M. Niemeyer, L. Mescheder, M. Pollefeys, and A. Geiger, "Convolutional occupancy networks," in *ECCV*. Springer, 2020, pp. 523–540. [3](#)
- [9] M. Niemeyer, L. Mescheder, M. Oechsle, and A. Geiger, "Differentiable volumetric rendering: Learning implicit 3d representations without 3d supervision," in *Proceedings of the IEEE/CVF Conference on Computer Vision and Pattern Recognition*, 2020, pp. 3504–3515. [3](#), [4](#), [7](#), [12](#), [16](#)
- [10] W. E. Lorensen and H. E. Cline, "Marching cubes: A high resolution 3d surface construction algorithm," *ACM siggraph computer graphics*, vol. 21, no. 4, pp. 163–169, 1987. [3](#), [18](#)
- [11] J. T. Kajiya and B. P. Von Herzen, "Ray tracing volume densities," *ACM SIGGRAPH computer graphics*, vol. 18, no. 3, pp. 165–174, 1984. [3](#), [12](#)
- [12] L. Liu, J. Gu, K. Z. Lin, T.-S. Chua, and C. Theobalt, "Neural sparse voxel fields," in *NeurIPS*, 2020. [3](#), [12](#), [13](#)
- [13] S. Lombardi, T. Simon, J. Saragih, G. Schwartz, A. Lehrmann, and Y. Sheikh, "Neural volumes: Learning dynamic renderable volumes from images," *TOG*, 2019. [3](#)
- [14] X. Wang and A. Gupta, "Generative image modeling using style and structure adversarial networks," in *European conference on computer vision*. Springer, 2016, pp. 318–335. [4](#), [7](#), [10](#), [11](#)
- [15] M. Gadelha, S. Maji, and R. Wang, "3d shape induction from 2d views of multiple objects," in *2017 International Conference on 3D Vision (3DV)*. IEEE, 2017, pp. 402–411. [4](#), [7](#), [16](#), [17](#)
- [16] V. Sitzmann, J. Thies, F. Heide, M. Nießner, G. Wetzstein, and M. Zollhofer, "Deepvoxels: Learning persistent 3d feature embeddings," in *Proceedings of the IEEE/CVF Conference on Computer Vision and Pattern Recognition*, 2019, pp. 2437–2446. [4](#), [5](#), [7](#), [12](#), [16](#)
- [17] J.-Y. Zhu, Z. Zhang, C. Zhang, J. Wu, A. Torralba, J. Tenenbaum, and B. Freeman, "Visual object networks: Image generation with disentangled 3d representations," *Advances in neural information processing systems*, vol. 31, 2018. [4](#), [7](#), [10](#), [16](#), [17](#)
- [18] T. Nguyen-Phuoc, C. Li, L. Theis, C. Richardt, and Y.-L. Yang, "HoloGAN: Unsupervised learning of 3D representations from natural images," in *ICCV*, 2019. [4](#), [6](#), [7](#), [16](#), [17](#), [18](#), [20](#)
- [19] V. Sitzmann, M. Zollhöfer, and G. Wetzstein, "Scene representation networks: Continuous 3d-structure-aware neural scene representations," *Advances in Neural Information Processing Systems*, vol. 32, 2019. [4](#), [7](#), [12](#), [16](#)
- [20] A. Jahanian, L. Chai, and P. Isola, "On the "steerability" of generative adversarial networks," in *ICLR*, 2020. [4](#), [7](#), [8](#)
- [21] A. Noguchi and T. Harada, "RGBD-GAN: Unsupervised 3d representation learning from natural image datasets via rgbd image synthesis," in *ICLR*, 2020. [4](#), [7](#), [10](#), [11](#)
- [22] T. Nguyen-Phuoc, C. Richardt, L. Mai, Y.-L. Yang, and N. Mitra, "BlockGAN: Learning 3D object-aware scene representations from unlabelled images," in *NeurIPS*, 2020. [4](#), [5](#), [6](#), [7](#), [16](#), [17](#), [18](#), [20](#)
- [23] A. Voynov and A. Babenko, "Unsupervised discovery of interpretable directions in the GAN latent space," in *ICML*, 2020. [4](#), [6](#), [7](#), [8](#)
- [24] A. Tewari, M. Elgharib, G. Bharaj, F. Bernard, H.-P. Seidel, P. Pérez, M. Zollhofer, and C. Theobalt, "StyleRig: Rigging StyleGAN for 3D control over portrait images," in *CVPR*, 2020. [4](#), [7](#), [9](#), [10](#)
- [25] M. Kowalski, S. J. Garbin, V. Estellers, T. Baltrušaitis, M. Johnson, and J. Shotton, "Config: Controllable neural face image generation," in *ECCV*, 2020, pp. 299–315. [4](#), [7](#), [9](#), [10](#)
- [26] H. Erik, H. Aaron, L. Jaakko, and P. Sylvain, "GANSpace: Discovering interpretable GAN controls," in *NeurIPS*, 2020. [4](#), [7](#), [8](#)
- [27] Y. Shen, J. Gu, X. Tang, and B. Zhou, "Interpreting the latent space of GANs for semantic face editing," in *CVPR*, 2020. [4](#), [6](#), [7](#)
- [28] X. Chen, D. Cohen-Or, B. Chen, and N. J. Mitra, "Towards a neural graphics pipeline for controllable image generation," in *Computer Graphics Forum*, vol. 40, no. 2. Wiley Online Library, 2021, pp. 127–140. [4](#), [7](#), [10](#), [11](#)
- [29] Y. Shen and B. Zhou, "Closed-form factorization of latent semantics in GANs," in *CVPR*, 2021. [4](#), [6](#), [7](#), [8](#)

- [30] K. Schwarz, Y. Liao, M. Niemeyer, and A. Geiger, "GRAF: Generative radiance fields for 3D-aware image synthesis," in *NeurIPS*, 2020. 4, 7, 16, 17, 18, 19
- [31] R. Martin-Brualla, N. Radwan, M. S. Sajjadi, J. T. Barron, A. Dosovitskiy, and D. Duckworth, "Nerf in the wild: Neural radiance fields for unconstrained photo collections," in *Proceedings of the IEEE/CVF Conference on Computer Vision and Pattern Recognition*, 2021, pp. 7210–7219. 4, 7, 14, 15, 16
- [32] A. Tewari, M. Elgharib, M. BR, F. Bernard, H.-P. Seidel, P. Pérez, M. Zöllhofer, and C. Theobalt, "Pie: Portrait image embedding for semantic control," *TOG*, vol. 39, no. 6, December 2020. 4, 7, 8, 9, 10
- [33] K. Zhang, G. Riegler, N. Snavely, and V. Koltun, "Nerf++: Analyzing and improving neural radiance fields," *arXiv preprint arXiv:2010.07492*, 2020. 4, 7, 15
- [34] M. Niemeyer and A. Geiger, "GIRAFFE: Representing scenes as compositional generative neural feature fields," in *CVPR*, 2021. 4, 5, 6, 7, 17, 18, 19, 20
- [35] A. Yu, V. Ye, M. Tancik, and A. Kanazawa, "pixelNeRF: Neural radiance fields from one or few images," in *Proceedings of the IEEE/CVF Conference on Computer Vision and Pattern Recognition*, 2021, pp. 4578–4587. 4, 7, 12, 13, 14, 16
- [36] A. Shoshan, N. Bhonker, I. Kviatkovsky, and G. Medioni, "GAN-control: Explicitly controllable GANs," in *ICCV*, 2021, pp. 14083–14093. 4, 7, 9, 10
- [37] Z. Wang, S. Wu, W. Xie, M. Chen, and V. A. Prisacariu, "NeRF-: Neural radiance fields without known camera parameters," *arXiv preprint arXiv:2102.07064*, 2021. 4, 7, 14, 15
- [38] C. Reiser, S. Peng, Y. Liao, and A. Geiger, "Kilonerf: Speeding up neural radiance fields with thousands of tiny mlps," in *Proceedings of the IEEE/CVF International Conference on Computer Vision*, 2021, pp. 14335–14345. 4, 7, 12, 13
- [39] J. T. Barron, B. Mildenhall, M. Tancik, P. Hedman, R. Martin-Brualla, and P. P. Srinivasan, "Mip-NeRF: A multiscale representation for anti-aliasing neural radiance fields," in *Proceedings of the IEEE/CVF International Conference on Computer Vision*, 2021, pp. 5855–5864. 4, 5, 7, 12, 16, 18
- [40] S. J. Garbin, M. Kowalski, M. Johnson, J. Shotton, and J. Valentin, "FastNeRF: High-fidelity neural rendering at 200fps," in *Proceedings of the IEEE/CVF International Conference on Computer Vision*, 2021, pp. 14346–14355. 4, 7, 12, 13, 16
- [41] M. Niemeyer and A. Geiger, "Campari: Camera-aware decomposed generative neural radiance fields," in *2021 International Conference on 3D Vision (3DV)*. IEEE, 2021, pp. 951–961. 4, 7
- [42] C.-H. Lin, W.-C. Ma, A. Torralba, and S. Lucey, "BARF: Bundle-adjusting neural radiance fields," in *IEEE International Conference on Computer Vision (ICCV)*, 2021. 4, 7, 12, 14, 16
- [43] M. C. Bühler, A. Meka, G. Li, T. Beeler, and O. Hilliges, "VariTex: Variational neural face textures," in *Proceedings of the IEEE/CVF International Conference on Computer Vision*, 2021, pp. 13890–13899. 4
- [44] Y. Liao, K. Schwarz, L. Mescheder, and A. Geiger, "Towards unsupervised learning of generative models for 3D controllable image synthesis," in *Proceedings of the IEEE/CVF conference on computer vision and pattern recognition*, 2020, pp. 5871–5880. 4, 7, 17
- [45] X. Pan, X. Xu, C. C. Loy, C. Theobalt, and B. Dai, "A shading-guided generative implicit model for shape-accurate 3d-aware image synthesis," in *NeurIPS*, 2021. 4, 7, 19, 20, 21
- [46] P. Zhou, L. Xie, B. Ni, and Q. Tian, "CIPS-3D: A 3d-aware generator of gans based on conditionally-independent pixel synthesis," *arXiv preprint arXiv:2110.09788*, 2021. 4, 5, 7, 18, 19
- [47] X. Xu, X. Pan, D. Lin, and B. Dai, "Generative occupancy fields for 3d surface-aware image synthesis," in *NeurIPS*, vol. 34, 2021, pp. 20683–20695. 4, 6, 7, 18, 19
- [48] D. Rebain, M. Matthews, K. M. Yi, D. Lagun, and A. Tagliasacchi, "LOLNeRF: Learn from one look," in *Proceedings of the IEEE/CVF Conference on Computer Vision and Pattern Recognition*, 2022, pp. 1558–1567. 4, 6, 7, 17, 18
- [49] K. Rematas, A. Liu, P. P. Srinivasan, J. T. Barron, A. Tagliasacchi, T. Funkhouser, and V. Ferrari, "Urban radiance fields," in *Proceedings of the IEEE/CVF Conference on Computer Vision and Pattern Recognition*, 2022, pp. 12932–12942. 4, 7, 12, 15, 16
- [50] E. R. Chan, C. Z. Lin, M. A. Chan, K. Nagano, B. Pan, S. D. Mello, O. Gallo, L. Guibas, J. Tremblay, S. Khamis, T. Karras, and G. Wetzstein, "Efficient Geometry-aware 3D Generative Adversarial Networks," in *Proceedings of the IEEE/CVF Conference on Computer Vision and Pattern Recognition*, 2022, pp. 16123–16133. 4, 6, 7, 11, 17, 18, 19, 20
- [51] Y. Deng, J. Yang, J. Xiang, and X. Tong, "GRAM: Generative Radiance Manifolds for 3D-Aware Image Generation," in *CVPR*, 2022. 4, 6, 7, 19
- [52] R. Or-El, X. Luo, M. Shan, E. Shechtman, J. J. Park, and I. Kemelmacher-Shlizerman, "StyleSDF: High-resolution 3d-consistent image and geometry generation," *CVPR*, 2022. 4, 6, 7, 17, 18, 19
- [53] Y. Xu, S. Peng, C. Yang, Y. Shen, and B. Zhou, "3D-aware Image Synthesis via Learning Structural and Textural Representations," in *CVPR*, 2022. 4, 6, 7, 18, 19
- [54] Z. Shi, Y. Shen, J. Zhu, D.-Y. Yeung, and Q. Chen, "3d-aware indoor scene synthesis with depth priors," in *ECCV*, 2022. 4, 6, 7, 10, 11
- [55] M. Tancik, V. Casser, X. Yan, S. Pradhan, B. Mildenhall, P. P. Srinivasan, J. T. Barron, and H. Kretschmar, "Block-nerf: Scalable large scene neural view synthesis," in *CVPR*, 2022, pp. 8248–8258. 4, 5, 7, 12, 15, 16
- [56] T. Müller, A. Evans, C. Schied, and A. Keller, "Instant neural graphics primitives with a multiresolution hash encoding," *ACM Transactions on Graphics*, 2022. 4, 7, 13
- [57] Y. Deng, J. Yang, D. Chen, F. Wen, and X. Tong, "Disentangled and controllable face image generation via 3D imitative-contrastive learning," in *Proceedings of the IEEE/CVF conference on computer vision and pattern recognition*, 2020, pp. 5154–5163. 4, 7, 8, 9, 10
- [58] X. Zhang, Z. Zheng, D. Gao, B. Zhang, P. Pan, and Y. Yang, "Multi-view consistent generative adversarial networks for 3D-aware image synthesis," in *Proceedings of the IEEE/CVF Conference on Computer Vision and Pattern Recognition*, 2022, pp. 18450–18459. 4, 7, 20
- [59] Y. Chen, Q. Wu, C. Zheng, T.-J. Cham, and J. Cai, "Sem2NeRF: Converting single-view semantic masks to neural radiance fields," in *ECCV*, 2022. 4, 7, 17, 21
- [60] A. Tewari, X. Pan, O. Fried, M. Agrawala, C. Theobalt *et al.*, "Disentangled3D: Learning a 3d generative model with disentangled geometry and appearance from monocular images," in *Proceedings of the IEEE/CVF Conference on Computer Vision and Pattern Recognition*, 2022, pp. 1516–1525. 4, 6, 7
- [61] K. Schwarz, A. Sauer, M. Niemeyer, Y. Liao, and A. Geiger, "VoxGRAF: Fast 3d-aware image synthesis with sparse voxel grids," in *NeurIPS*, 2022. 4, 7, 18, 19, 20
- [62] I. Skorokhodov, S. Tulyakov, Y. Wang, and P. Wonka, "EpiGRAF: Rethinking training of 3D gans," in *NeurIPS*, 2022. 4, 5, 6, 7, 18, 19
- [63] J. Sun, X. Wang, Y. Shi, L. Wang, J. Wang, and Y. Liu, "IDE-3D: Interactive disentangled editing for high-resolution 3D-aware portrait synthesis," in *SIGGRAPH Asia 2022*, 2022. 4, 7, 17, 18, 20, 21
- [64] X. Zhao, F. Ma, D. Güera, Z. Ren, A. G. Schwing, and A. Colburn, "Generative multiplane images: Making a 2d gan 3d-aware," in *ECCV*, 2022. 4, 7, 18
- [65] J.-g. Kwak, Y. Li, D. Yoon, D. Kim, D. Han, and H. Ko, "Injecting 3d perception of controllable nerf-gan into stylegan for editable portrait image synthesis," in *ECCV*, 2022. 4, 7, 20
- [66] Y. Liu, Z. Shu, Y. Li, Z. Lin, R. Zhang, and S. Kung, "3d-fm gan: Towards 3d-controllable face manipulation," in *ECCV*, 2022. 4, 7, 9, 10
- [67] R. Jensen, A. Dahl, G. Vogiatzis, E. Tola, and H. Aanaes, "Large scale multi-view stereopsis evaluation," in *Proceedings of the IEEE conference on computer vision and pattern recognition*, 2014, pp. 406–413. 4, 5
- [68] A. Chen, Z. Xu, F. Zhao, X. Zhang, F. Xiang, J. Yu, and H. Su, "Mvsnerf: Fast generalizable radiance field reconstruction from multi-view stereo," in *Proceedings of the IEEE/CVF International Conference on Computer Vision*, 2021, pp. 14124–14133. 5, 12, 13, 14, 16
- [69] S. Cai, A. Obukhov, D. Dai, and L. Van Gool, "Pix2NeRF: Unsupervised conditional p-GAN for single image to neural radiance fields translation," in *Proceedings of the IEEE/CVF Conference on Computer Vision and Pattern Recognition*, 2022, pp. 3981–3990. 5, 6, 7, 17, 21
- [70] L. Yang, P. Luo, C. Change Loy, and X. Tang, "A large-scale car dataset for fine-grained categorization and verification," in *Proceedings of the IEEE conference on computer vision and pattern recognition*, 2015, pp. 3973–3981. 4, 5, 6

- [71] Y. Jeong, S. Ahn, C. Choy, A. Anandkumar, M. Cho, and J. Park, "Self-calibrating neural radiance fields," in *Proceedings of the IEEE/CVF International Conference on Computer Vision*, 2021, pp. 5846–5854. [5](#), [14](#)
- [72] Y. Jin, D. Mishkin, A. Mishchuk, J. Matas, P. Fua, K. M. Yi, and E. Trulls, "Image matching across wide baselines: From paper to practice," *International Journal of Computer Vision*, vol. 129, no. 2, pp. 517–547, 2021. [4](#), [5](#)
- [73] R. Martin-Brualla, N. Radwan, M. S. Sajjadi, J. T. Barron, A. Dosovitskiy, and D. Duckworth, "Nerf in the wild: Neural radiance fields for unconstrained photo collections," in *CVPR*, 2021. [4](#), [5](#), [12](#), [16](#)
- [74] J. L. Schonberger and J.-M. Frahm, "Structure-from-motion revisited," in *Proceedings of the IEEE conference on computer vision and pattern recognition*, 2016, pp. 4104–4113. [4](#), [14](#), [17](#)
- [75] A. Dai, A. X. Chang, M. Savva, M. Halber, T. Funkhouser, and M. Nießner, "ScanNet: Richly-annotated 3d reconstructions of indoor scenes," in *Proceedings of the IEEE conference on computer vision and pattern recognition*, 2017, pp. 5828–5839. [4](#)
- [76] A. X. Chang, T. Funkhouser, L. Guibas, P. Hanrahan, Q. Huang, Z. Li, S. Savarese, M. Savva, S. Song, H. Su *et al.*, "Shapenet: An information-rich 3d model repository," *arXiv preprint arXiv:1512.03012*, 2015. [4](#)
- [77] B. Mildenhall, P. P. Srinivasan, R. Ortiz-Cayon, N. K. Kalantari, R. Ramamoorthi, R. Ng, and A. Kar, "Local light field fusion: Practical view synthesis with prescriptive sampling guidelines," *ACM Transactions on Graphics (TOG)*, vol. 38, no. 4, pp. 1–14, 2019. [4](#)
- [78] A. Knapitsch, J. Park, Q.-Y. Zhou, and V. Koltun, "Tanks and temples: Benchmarking large-scale scene reconstruction," *ACM Transactions on Graphics (ToG)*, vol. 36, no. 4, pp. 1–13, 2017. [4](#)
- [79] T. Karras, S. Laine, and T. Aila, "A style-based generator architecture for generative adversarial networks," in *CVPR*, 2019, pp. 4401–4410. [4](#), [6](#), [9](#), [10](#), [21](#)
- [80] Y. Choi, Y. Uh, J. Yoo, and J.-W. Ha, "StarGAN v2: Diverse image synthesis for multiple domains," in *CVPR*, 2020. [4](#), [6](#)
- [81] T. Karras, M. Aittala, J. Hellsten, S. Laine, J. Lehtinen, and T. Aila, "Training generative adversarial networks with limited data," in *NeurIPS*, 2020. [4](#), [6](#), [9](#), [10](#), [21](#)
- [82] F. Yu, Y. Zhang, S. Song, A. Seff, and J. Xiao, "Lsun: Construction of a large-scale image dataset using deep learning with humans in the loop," *arXiv preprint arXiv:1506.03365*, 2015. [4](#), [5](#), [6](#)
- [83] J. Johnson, B. Hariharan, L. Van Der Maaten, L. Fei-Fei, C. Lawrence Zitnick, and R. Girshick, "CLEVR: A diagnostic dataset for compositional language and elementary visual reasoning," in *Proceedings of the IEEE conference on computer vision and pattern recognition*, 2017, pp. 2901–2910. [4](#), [5](#), [6](#)
- [84] Z. Liu, P. Luo, X. Wang, and X. Tang, "Deep learning face attributes in the wild," in *ICCV*, 2015. [4](#), [6](#)
- [85] T. Karras, T. Aila, S. Laine, and J. Lehtinen, "Progressive growing of GANs for improved quality, stability, and variation," in *ICLR*, 2018. [4](#), [6](#), [18](#)
- [86] A. Dosovitskiy, G. Ros, F. Codevilla, A. Lopez, and V. Koltun, "CARLA: An open urban driving simulator," in *Conference on Robot Learning*, 2017, pp. 1–16. [4](#), [6](#)
- [87] T. Salimans, I. Goodfellow, W. Zaremba, V. Cheung, A. Radford, and X. Chen, "Improved techniques for training GANs," in *NeurIPS*, 2016. [5](#)
- [88] M. Heusel, H. Ramsauer, T. Unterthiner, B. Nessler, and S. Hochreiter, "GANs trained by a two time-scale update rule converge to a local Nash equilibrium," in *NeurIPS*, 2017. [5](#)
- [89] M. Bińkowski, D. J. Sutherland, M. Arbel, and A. Gretton, "Demystifying mmd gans," *arXiv preprint arXiv:1801.01401*, 2018. [5](#)
- [90] R. Zhang, P. Isola, A. A. Efros, E. Shechtman, and O. Wang, "The unreasonable effectiveness of deep features as a perceptual metric," in *CVPR*, 2018, pp. 586–595. [5](#)
- [91] C. Szegedy, V. Vanhoucke, S. Ioffe, J. Shlens, and Z. Wojna, "Rethinking the inception architecture for computer vision," in *CVPR*, 2016, pp. 2818–2826. [5](#)
- [92] J. Deng, W. Dong, R. Socher, L.-J. Li, K. Li, and L. Fei-Fei, "Imagenet: A large-scale hierarchical image database," in *CVPR*, 2009, pp. 248–255. [5](#)
- [93] K. Simonyan and A. Zisserman, "Very deep convolutional networks for large-scale image recognition," in *ICLR*, 2015. [5](#)
- [94] Z. Wang, A. C. Bovik, H. R. Sheikh, and E. P. Simoncelli, "Image quality assessment: From error visibility to structural similarity," *TIP*, vol. 13, 2004. [5](#), [6](#)
- [95] J. Deng, J. Guo, N. Xue, and S. Zafeiriou, "ArcFace: Additive angular margin loss for deep face recognition," in *CVPR*, 2019. [6](#)
- [96] Y. Shi, D. Aggarwal, and A. K. Jain, "Lifting 2d stylegan for 3d-aware face generation," in *Proceedings of the IEEE/CVF Conference on Computer Vision and Pattern Recognition*, 2021, pp. 6258–6266. [7](#), [10](#), [11](#)
- [97] A. Pumarola, E. Corona, G. Pons-Moll, and F. Moreno-Noguer, "D-NeRF: Neural radiance fields for dynamic scenes," in *Proceedings of the IEEE/CVF Conference on Computer Vision and Pattern Recognition*, 2021, pp. 10318–10327. [7](#), [15](#), [16](#)
- [98] K. Park, U. Sinha, J. T. Barron, S. Bouaziz, D. B. Goldman, S. M. Seitz, and R. Martin-Brualla, "Nerfies: Deformable neural radiance fields," in *Proceedings of the IEEE/CVF International Conference on Computer Vision*, 2021, pp. 5865–5874. [7](#), [15](#), [16](#)
- [99] V. Sitzmann, S. Rezkikov, B. Freeman, J. Tenenbaum, and F. Durand, "Light field networks: Neural scene representations with single-evaluation rendering," *Advances in Neural Information Processing Systems*, vol. 34, pp. 19313–19325, 2021. [7](#), [12](#), [13](#), [14](#), [16](#)
- [100] M. S. Sajjadi, H. Meyer, E. Pot, U. Bergmann, K. Greff, N. Radwan, S. Vora, M. Lučić, D. Duckworth, A. Dosovitskiy *et al.*, "Scene representation transformer: Geometry-free novel view synthesis through set-latent scene representations," in *Proceedings of the IEEE/CVF Conference on Computer Vision and Pattern Recognition*, 2022, pp. 6229–6238. [7](#), [12](#), [13](#), [14](#), [16](#)
- [101] Y. Xiangli, L. Xu, X. Pan, N. Zhao, A. Rao, C. Theobalt, B. Dai, and D. Lin, "BungeeNeRF: Progressive neural radiance field for extreme multi-scale scene rendering," in *The European Conference on Computer Vision (ECCV)*, 2022. [7](#), [12](#), [15](#)
- [102] D. Watson, W. Chan, R. Martin-Brualla, J. Ho, A. Tagliasacchi, and M. Norouzi, "Novel view synthesis with diffusion models," *arXiv preprint arXiv:2210.04628*, 2022. [7](#), [16](#), [17](#)
- [103] T. Karras, S. Laine, M. Aittala, J. Hellsten, J. Lehtinen, and T. Aila, "Analyzing and improving the image quality of StyleGAN," in *CVPR*, 2020. [6](#), [9](#), [10](#), [21](#)
- [104] T. Karras, M. Aittala, S. Laine, E. Härkönen, J. Hellsten, J. Lehtinen, and T. Aila, "Alias-free generative adversarial networks," in *NeurIPS*, 2021. [6](#), [21](#)
- [105] W. Xia, Y. Zhang, Y. Yang, J.-H. Xue, B. Zhou, and M.-H. Yang, "GAN inversion: A survey," *TPAMI*, 2022. [6](#), [20](#), [21](#)
- [106] S. Nurit, B. Ron, and M. Tomer, "GAN steerability without optimization," in *ICLR*, 2021. [6](#), [8](#)
- [107] R. Abdal, P. Zhu, N. Mitra, and P. Wonka, "StyleFlow: Attribute-conditioned exploration of StyleGAN-generated images using conditional continuous normalizing flows," *TOG*, 2021. [6](#), [7](#), [8](#), [21](#)
- [108] A. Plumerault, H. L. Borgne, and C. Hudelot, "Controlling generative models with continuous factors of variations," in *ICLR*, 2020. [7](#)
- [109] P. Paysan, R. Knothe, B. Amberg, S. Romdhani, and T. Vetter, "A 3d face model for pose and illumination invariant face recognition," in *2009 sixth IEEE international conference on advanced video and signal based surveillance*. Ieee, 2009, pp. 296–301. [8](#), [9](#)
- [110] Y. Hong, B. Peng, H. Xiao, L. Liu, and J. Zhang, "HeadNeRF: A real-time nerf-based parametric head model," in *Proceedings of the IEEE/CVF Conference on Computer Vision and Pattern Recognition*, 2022, pp. 20374–20384. [8](#)
- [111] K. Sun, S. Wu, Z. Huang, N. Zhang, Q. Wang, and H. Li, "Controllable 3d face synthesis with conditional generative occupancy fields," in *NeurIPS*, 2022. [8](#)
- [112] N. Ruiz, E. Chong, and J. M. Rehg, "Fine-grained head pose estimation without keypoints," in *Proceedings of the IEEE conference on computer vision and pattern recognition workshops*, 2018, pp. 2074–2083. [9](#)
- [113] R. Ramamoorthi and P. Hanrahan, "An efficient representation for irradiance environment maps," in *Proceedings of the 28th annual conference on Computer graphics and interactive techniques*, 2001, pp. 497–500. [9](#)
- [114] A. Tewari, M. Zollhofer, H. Kim, P. Garrido, F. Bernard, P. Perez, and C. Theobalt, "MoFA: Model-based deep convolutional face autoencoder for unsupervised monocular reconstruction," in *Proceedings of the IEEE International Conference on Computer Vision Workshops*, 2017, pp. 1274–1283. [9](#)

- [115] J. Wu, C. Zhang, T. Xue, B. Freeman, and J. Tenenbaum, "Learning a probabilistic latent space of object shapes via 3d generative-adversarial modeling," *Advances in neural information processing systems*, vol. 29, 2016. 10
- [116] H. Abu Alhaija, S. K. Mustikovela, A. Geiger, and C. Rother, "Geometric image synthesis," in *Asian Conference on Computer Vision*, 2018, pp. 85–100. 10, 11
- [117] W. Jang and L. Agapito, "CodeNeRF: Disentangled neural radiance fields for object categories," in *Proceedings of the IEEE/CVF International Conference on Computer Vision*, 2021, pp. 12949–12958. 12, 13, 16
- [118] A. R. Kosiorek, H. Strathmann, D. Zoran, P. Moreno, R. Schneider, S. Mokrá, and D. J. Rezende, "NeRF-VAE: A geometry aware 3D scene generative model," in *International Conference on Machine Learning*. PMLR, 2021, pp. 5742–5752. 12, 13, 16
- [119] V. Sitzmann, E. Chan, R. Tucker, N. Snavely, and G. Wetzstein, "MetaSDF: Meta-learning signed distance functions," *Advances in Neural Information Processing Systems*, vol. 33, pp. 10 136–10 147, 2020. 12
- [120] M. Oechsle, L. Mescheder, M. Niemeyer, T. Strauss, and A. Geiger, "Texture fields: Learning texture representations in function space," in *Proceedings of the IEEE/CVF International Conference on Computer Vision*, 2019, pp. 4531–4540. 12
- [121] A. Yu, R. Li, M. Tancik, H. Li, R. Ng, and A. Kanazawa, "Plenotrees for real-time rendering of neural radiance fields," in *Proceedings of the IEEE/CVF International Conference on Computer Vision*, 2021, pp. 5752–5761. 12, 13
- [122] T. Hu, S. Liu, Y. Chen, T. Shen, and J. Jia, "EfficientNeRF: Efficient neural radiance fields," in *Proceedings of the IEEE/CVF Conference on Computer Vision and Pattern Recognition*, 2022, pp. 12902–12911. 12, 13
- [123] A. Jain, M. Tancik, and P. Abbeel, "Putting nerf on a diet: Semantically consistent few-shot view synthesis," in *Proceedings of the IEEE/CVF International Conference on Computer Vision*, 2021, pp. 5885–5894. 12, 14, 16
- [124] Y. Liu, S. Peng, L. Liu, Q. Wang, P. Wang, C. Theobalt, X. Zhou, and W. Wang, "Neural rays for occlusion-aware image-based rendering," in *Proceedings of the IEEE/CVF Conference on Computer Vision and Pattern Recognition*, 2022, pp. 7824–7833. 12, 14
- [125] G. Gafni, J. Thies, M. Zollhofer, and M. Nießner, "Dynamic neural radiance fields for monocular 4d facial avatar reconstruction," in *Proceedings of the IEEE/CVF Conference on Computer Vision and Pattern Recognition*, 2021, pp. 8649–8658. 12, 15, 16
- [126] Q. Wang, Z. Wang, K. Genova, P. P. Srinivasan, H. Zhou, J. T. Barron, R. Martin-Brualla, N. Snavely, and T. Funkhouser, "IBRNet: Learning multi-view image-based rendering," in *Proceedings of the IEEE/CVF Conference on Computer Vision and Pattern Recognition*, 2021, pp. 4690–4699. 13, 16
- [127] A. Trevisan and B. Yang, "GRF: Learning a general radiance field for 3D representation and rendering," in *Proceedings of the IEEE/CVF International Conference on Computer Vision*, 2021, pp. 15 182–15 192. 13, 16
- [128] P. Hedman, P. P. Srinivasan, B. Mildenhall, J. T. Barron, and P. Debevec, "Baking neural radiance fields for real-time view synthesis," in *Proceedings of the IEEE/CVF International Conference on Computer Vision*, 2021, pp. 5875–5884. 13
- [129] D. B. Lindell, J. N. Martel, and G. Wetzstein, "Autoint: Automatic integration for fast neural volume rendering," in *Proceedings of the IEEE/CVF Conference on Computer Vision and Pattern Recognition*, 2021, pp. 14556–14565. 13
- [130] L. Wu, J. Y. Lee, A. Bhattad, Y.-X. Wang, and D. Forsyth, "DIVER: Real-time and accurate neural radiance fields with deterministic integration for volume rendering," in *Proceedings of the IEEE/CVF Conference on Computer Vision and Pattern Recognition*, 2022, pp. 16 200–16 209. 13
- [131] M. M. Johari, Y. Lepoittevin, and F. Fleuret, "GeoNeRF: Generalizing nerf with geometry priors," in *Proceedings of the IEEE/CVF Conference on Computer Vision and Pattern Recognition*, 2022, pp. 18 365–18 375. 14
- [132] X. Zhang, S. Bi, K. Sunkavalli, H. Su, and Z. Xu, "NeRFusion: Fusing radiance fields for large-scale scene reconstruction," in *Proceedings of the IEEE/CVF Conference on Computer Vision and Pattern Recognition*, 2022, pp. 5449–5458. 14
- [133] M. Niemeyer, J. T. Barron, B. Mildenhall, M. S. Sajjadi, A. Geiger, and N. Radwan, "Regnerf: Regularizing neural radiance fields for view synthesis from sparse inputs," in *Proceedings of the IEEE/CVF Conference on Computer Vision and Pattern Recognition*, 2022, pp. 5480–5490. 14
- [134] D. Xu, Y. Jiang, P. Wang, Z. Fan, H. Shi, and Z. Wang, "SinNeRF: Training neural radiance fields on complex scenes from a single image," in *ECCV*, 2022. 14
- [135] K. Deng, A. Liu, J.-Y. Zhu, and D. Ramanan, "Depth-supervised nerf: Fewer views and faster training for free," in *Proceedings of the IEEE/CVF Conference on Computer Vision and Pattern Recognition*, 2022, pp. 12 882–12 891. 14
- [136] B. Roessle, J. T. Barron, B. Mildenhall, P. P. Srinivasan, and M. Nießner, "Dense depth priors for neural radiance fields from sparse input views," in *Proceedings of the IEEE/CVF Conference on Computer Vision and Pattern Recognition*, 2022, pp. 12 892–12 901. 14
- [137] S.-Y. Su, F. Yu, M. Zollhofer, and H. Rhodin, "A-NeRF: Articulated neural radiance fields for learning human shape, appearance, and pose," *Advances in Neural Information Processing Systems*, vol. 34, pp. 12 278–12 291, 2021. 14
- [138] Q. Meng, A. Chen, H. Luo, M. Wu, H. Su, L. Xu, X. He, and J. Yu, "GNeRF: GAN-based neural radiance field without posed camera," in *Proceedings of the IEEE/CVF International Conference on Computer Vision*, 2021, pp. 6351–6361. 14
- [139] Y.-C. Guo, D. Kang, L. Bao, Y. He, and S.-H. Zhang, "NeRFReN: Neural radiance fields with reflections," in *Proceedings of the IEEE/CVF Conference on Computer Vision and Pattern Recognition*, 2022, pp. 18 409–18 418. 14
- [140] D. Derksen and D. Izzo, "Shadow neural radiance fields for multi-view satellite photogrammetry," in *Proceedings of the IEEE/CVF Conference on Computer Vision and Pattern Recognition*, 2021, pp. 1152–1161. 15
- [141] H. Turki, D. Ramanan, and M. Satyanarayanan, "Mega-NeRF: Scalable construction of large-scale nerfs for virtual fly-throughs," in *Proceedings of the IEEE/CVF Conference on Computer Vision and Pattern Recognition (CVPR)*, June 2022, pp. 12 922–12 931. 15
- [142] L. Wang, J. Zhang, X. Liu, F. Zhao, Y. Zhang, Y. Zhang, M. Wu, J. Yu, and L. Xu, "Fourier plenotrees for dynamic radiance field rendering in real-time," in *Proceedings of the IEEE/CVF Conference on Computer Vision and Pattern Recognition*, 2022, pp. 13 524–13 534. 15, 16
- [143] K. Park, U. Sinha, P. Hedman, J. T. Barron, S. Bouaziz, D. B. Goldman, R. Martin-Brualla, and S. M. Seitz, "HyperNeRF: A higher-dimensional representation for topologically varying neural radiance fields," *TOG*, 2021. 15, 16
- [144] W. Xian, J.-B. Huang, J. Kopf, and C. Kim, "Space-time neural irradiance fields for free-viewpoint video," in *Proceedings of the IEEE/CVF Conference on Computer Vision and Pattern Recognition*, 2021, pp. 9421–9431. 15
- [145] Z. Li, S. Niklaus, N. Snavely, and O. Wang, "Neural scene flow fields for space-time view synthesis of dynamic scenes," in *Proceedings of the IEEE/CVF Conference on Computer Vision and Pattern Recognition*, 2021, pp. 6498–6508. 15
- [146] E. Tretschk, A. Tewari, V. Golyanik, M. Zollhofer, C. Lassner, and C. Theobalt, "Non-rigid neural radiance fields: Reconstruction and novel view synthesis of a dynamic scene from monocular video," in *Proceedings of the IEEE/CVF International Conference on Computer Vision*, 2021, pp. 12 959–12 970. 15, 16
- [147] Y. Du, Y. Zhang, H.-X. Yu, J. B. Tenenbaum, and J. Wu, "Neural radiance flow for 4d view synthesis and video processing," in *2021 IEEE/CVF International Conference on Computer Vision (ICCV)*. IEEE Computer Society, 2021, pp. 14 304–14 314. 15, 16
- [148] K. Kania, K. M. Yi, M. Kowalski, T. Trzciński, and A. Tagliasacchi, "CoNeRF: Controllable neural radiance fields," in *Proceedings of the IEEE/CVF Conference on Computer Vision and Pattern Recognition*, 2022, pp. 18 623–18 632. 15, 16
- [149] P. Henzler, N. J. Mitra, and T. Ritschel, "Escaping Plato's cave: 3D shape from adversarial rendering," in *ICCV*, 2019. 16, 17
- [150] J. Sun, X. Wang, Y. Zhang, X. Li, Q. Zhang, Y. Liu, and J. Wang, "FENeRF: Face editing in neural radiance fields," in *Proceedings of the IEEE Conference on Computer Vision and Pattern Recognition (CVPR)*, 2022. 17, 20, 21
- [151] N. Müller, A. Simonelli, L. Porzi, S. R. Bulò, M. Nießner, and P. Kotschieder, "AutoRF: Learning 3d object radiance fields from single view observations," in *Proceedings of the IEEE/CVF Conference on Computer Vision and Pattern Recognition*, 2022, pp. 3971–3980. 17, 21

- [152] C. Z. Lin, D. B. Lindell, E. R. Chan, and G. Wetzstein, "3d GAN inversion for controllable portrait image animation," in *ECCV Workshop on Learning to Generate 3D Shapes and Scenes*, 2022. 17, 20, 21
- [153] J. Ho, A. Jain, and P. Abbeel, "Denoising diffusion probabilistic models," in *Advances in Neural Information Processing Systems*, vol. 33, 2020, pp. 6840–6851. 17
- [154] Y. Song and S. Ermon, "Generative modeling by estimating gradients of the data distribution," in *Advances in Neural Information Processing Systems*, vol. 32, 2019. 17
- [155] Y. Song, J. Sohl-Dickstein, D. P. Kingma, A. Kumar, S. Ermon, and B. Poole, "Score-based generative modeling through stochastic differential equations," in *ICLR*, 2020. 17
- [156] P. Dhariwal and A. Nichol, "Diffusion models beat gans on image synthesis," in *Advances in Neural Information Processing Systems*, vol. 34, 2021, pp. 8780–8794. 17
- [157] J. Song, C. Meng, and S. Ermon, "Denoising diffusion implicit models," in *ICLR*, 2021. 17
- [158] R. Rombach, A. Blattmann, D. Lorenz, P. Esser, and B. Ommer, "High-resolution image synthesis with latent diffusion models," in *Proceedings of the IEEE/CVF Conference on Computer Vision and Pattern Recognition*, 2022, pp. 10 684–10 695. 17
- [159] P. Bojanowski, A. Joulin, D. Lopez-Paz, and A. Szlam, "Optimizing the latent space of generative networks," *arXiv preprint arXiv:1707.05776*, 2017. 17, 18
- [160] I. Goodfellow, J. Pouget-Abadie, M. Mirza, B. Xu, D. Warde-Farley, S. Ozair, A. Courville, and Y. Bengio, "Generative adversarial networks," *Communications of the ACM*, vol. 63, no. 11, pp. 139–144, 2020. 17, 18
- [161] V. Sitzmann, J. N. Martel, A. W. Bergman, D. B. Lindell, and G. Wetzstein, "Implicit neural representations with periodic activation functions," in *NeurIPS*, 2020. 18
- [162] Y. Xue, Y. Li, K. K. Singh, and Y. J. Lee, "GIRAFFE-HD: A high-resolution 3d-aware generative model," in *Proceedings of the IEEE Conference on Computer Vision and Pattern Recognition (CVPR)*, 2022. 18, 19, 20
- [163] Z. Shi, Y. Xu, Y. Shen, D. Zhao, Q. Chen, and D.-Y. Yeung, "Improving 3d-aware image synthesis with a geometry-aware discriminator," in *NeurIPS*, 2022. 20
- [164] D. Roich, R. Mokady, A. H. Bermano, and D. Cohen-Or, "Pivotal tuning for latent-based editing of real images," *TOG*, 2022. 21
- [165] B. Zhang, S. Gu, B. Zhang, J. Bao, D. Chen, F. Wen, Y. Wang, and B. Guo, "Styleswin: Transformer-based gan for high-resolution image generation," in *CVPR*, 2022. 21
- [166] A. Sauer, K. Schwarz, and A. Geiger, "StyleGAN-XL: Scaling StyleGAN to large diverse datasets," in *ACM SIGGRAPH 2022 Conference Proceedings*, 2022, pp. 1–10. 22
- [167] R. Mokady, O. Tov, M. Yarom, O. Lang, I. Mosseri, T. Dekel, D. Cohen-Or, and M. Irani, "Self-distilled StyleGAN: Towards generation from internet photos," in *ACM SIGGRAPH 2022 Conference Proceedings*, 2022, pp. 1–9. 22